UCanWBGT: urban street canyon heat stress calculation for weather and climate models

Shonk, J. K. P. ORCID: https://orcid.org/0000-0003-0479-7590, Blunn, L. P. ORCID: https://orcid.org/0000-0002-3207-5002, Kumar, V. ORCID: https://orcid.org/0000-0002-7395-4548, Wurtz, J. ORCID: https://orcid.org/0000-0002-8195-3537 and Masson, V. (2026) UCanWBGT: urban street canyon heat stress calculation for weather and climate models. Quarterly Journal of the Royal Meteorological Society. e70082. ISSN 1477-870X doi: 10.1002/qj.70082 Available at https://centaur.reading.ac.uk/128313/

Received: 2 April 2025 | Revised: 11 November 2025 | Accepted: 12 November 2025

DOI: 10.1002/qj.70082

Quarterly Journal of the Royal Meteorological Society RMetS

RESEARCH ARTICLE

UCanWBGT: urban street canyon heat stress calculation for weather and climate models

Jonathan K. P. Shonk[1] | **Lewis P. Blunn**[1] | **Vinod Kumar**[2] | **Jean Wurtz**[3] | **Valéry Masson**[3]

[1]MetOffice@Reading, University of Reading, Reading, UK

[2]Bureau of Meteorology, Melbourne, Victoria, Australia

[3]Météo France, Toulouse, France

Correspondence
Jonathan K. P. Shonk,
MetOffice@Reading, University of Reading, Reading, UK.
Email: jon.shonk@metoffice.gov.uk

Funding information
MetOffice, AI4 Climate project, supported by the UK Department of Science, Innovation and Technology (DSIT); Weather and Climate Science for Service Partnership (WCSSP) India project, supported by the UK Department of Science, Innovation and Technology (DSIT).

ABSTRACT

We present UCanWBGT, a heat stress model for estimating wet-bulb globe temperature (WBGT) in an infinitely long street canyon. Radiative transfer within the canyon is calculated analytically from downward fluxes and surface temperature to determine the mean radiant temperature for a black globe. In combination with a standard set of meteorological fields, WBGT is determined via an empirical equation, resulting in a computationally efficient approach suitable for inclusion in numerical weather prediction (NWP) and climate models. For validation, we apply UCanWBGT to high-resolution NWP output over Paris during a heatwave event and compare this with WBGT values derived from black-globe thermometer observations made in street canyons during the PANAME project. UCanWBGT performs well, capturing daily variations in WBGT and representing transitions between sunlit and shaded conditions. Discrepancies are linked to forecast errors in meteorological fields and assumptions associated with the street canyon. Sensitivity tests reveal that modifying the canyon geometry affects the degree (and timing) of shading experienced in the canyon, and neglecting the urban geometry (representing it as a flat plane) eliminates the representation of daytime shading and reduces WBGT enhancement via reflections within the canyon. WBGT is also highly sensitive to meteorological fields, particularly temperature and humidity, although less so to the albedo and emissivity of the canyon facets. We conclude by demonstrating a practical application of UCanWBGT. Using NWP simulations for August 10, 2024, we estimate WBGT along the marathon route at the 2024 Paris Olympics and, using published safety thresholds, identify timing and routing strategies that minimise heat-stress risks for athletes. We identify a period of high risk through the middle of the day, noting that the event would best be scheduled outside this period. Also, for daytime events, increased routing through urban areas and forest roads reduces risk, while for nighttime events rural areas are preferable.

KEYWORDS

heat stress, NWP models, radiative transfer, urban canyon, wet-bulb globe temperature

1 | BACKGROUND

Hot weather has the potential to be hazardous to human health, especially in urban areas, where an increasing percentage of the global population lives. The societal impacts of recent heatwaves have been well documented (Campbell *et al.*, 2018; García-Herrera *et al.*, 2010; Shaposhnikov *et al.*, 2014) and many studies have indicated that heatwave events are projected to increase in severity and frequency in future climates (Aadhar & Mishra, 2023; Horton *et al.*, 2016; IPCC, 2023; Meehl & Tebaldi, 2004). There is therefore a need to provide adequate, usable forecasts of heatwave conditions in terms of the potential impacts on human health. In this work, we aim to develop a method to determine heat stress in urban areas that is suitable for use operationally in a numerical weather prediction (NWP) or climate model.

The human impact of heat stress arises from four meteorological fields: air temperature, humidity, wind speed, and incident radiation flux (shortwave and longwave). Over the years, these fields have been combined in many ways into indices with the aim of quantifying heat stress in a single value (Błazejczyk *et al.*, 2012; Buzan *et al.*, 2015). Two widely used indices that include the effects of all four relevant fields are wet-bulb globe temperature (WBGT: Yaglou & Minard, 1957; Parsons, 2006, 2013) and Universal Thermal Climate Index (UTCI: Fiala *et al.*, 2010, 2012). Both of these indices define the radiative impact using mean radiant temperature (MRT), the emission temperature of a target object when it is in radiative equilibrium with its environment.

Modelling MRT, particularly in urban environments, is highly complex and computationally challenging (Kántor & Unger, 2011). Typically, incident radiation on the target object is determined by modelling the surroundings as a number of facets that are emitting or reflecting radiation and summing the total radiation across these facets, weighted by the solid angle subtended by each facet (Fanger, 1972; Jendritzky & Nübler, 1981). Directional weighting is needed for this sum if the target is non-spherical—for example, a model of a standing person (as used in UTCI) projects a greater fraction of its surface area to radiation incident from the sides than it does to radiation from above. For a spherical target (as used in WBGT), radiation is received equally from all directions. Dedicated models have been developed that can calculate MRT from any urban geometry: the RayMan model of Matzarakis *et al.* (2010) performs a spherical integration across any number of facets to calculate the incident radiation; the SOLWEIG model of Lindberg *et al.* (2008) combines radiation from facets into streams from six directions (from above and below, and from north, south, east, and west).

For use in an NWP or climate model, we require a computationally simple solution to calculate MRT. Given that the majority of urban surface schemes treat urban areas as infinitely long street canyons (Lipson *et al.*, 2024), we will develop our model for this morphology. While it is possible to apply RayMan and SOLWEIG (and indeed more complex methods, such as ENVI-Met: Bruse, 1999) to simpler geometries such as street canyons, they are bespoke models designed to calculate MRT in complex, three-dimensional urban geometries and are therefore unnecessarily complex for our purposes (and also likely too computationally expensive for large NWP domains). Bespoke canyon MRT models have been developed, such as the SURM model (Fischereit, 2021). However, this represents the target of the MRT calculation as person-shaped, hence numerical integration is needed to determine the viewing factors that distribute radiation within the canyon. The models of Krayenhoff *et al.* (2014) and Park *et al.* (2018) calculate MRT in a street canyon and can include trees but use a Monte Carlo approach, which also tends to be computationally expensive.

An advantage of using a canyon morphology is that, in principle, the geometry is so simple that we can describe the transfer of radiation around the canyon using analytical equations, hence there is no reliance on empirical relationships or numerical integration. Several studies present equations that describe the transfer of radiation within a street canyon (Kusaka *et al.*, 2001; Masson, 2000; Oleson *et al.*, 2008; Wang *et al.*, 2013), upon which we can base our model. Furthermore, rather than modelling the target as a representation of a person (like Fischereit, 2021), we can represent it as a black-globe thermometer by selecting WBGT as our heat stress metric. While the equations defining WBGT are empirical (Parsons, 2006; see Section 2.7), we can calculate MRT entirely analytically, therefore maximising computational efficiency. A caveat on the use of WBGT is that does not include human physiological factors, such as metabolic rate and clothing insulation, in contrast to more detailed indices such as UTCI. However, WBGT has been widely studied as a heat stress metric and, despite this caveat, established WBGT safety thresholds have been defined for certain activities, including long-distance running (the American College of Sports Medicine: Armstrong *et al.*, 1996).

Our heat stress calculation method should also rely solely on variables typically calculated and stored during NWP or climate simulations. Di Napoli *et al.* (2020) developed a method to calculate MRT for a person standing on a flat surface using standard NWP output fields. The incident radiation on the target is therefore an equally weighted sum of downward radiation from the sky and upward radiation reflected or emitted from the ground. However, this approach is not applicable within an urban

environment, where radiation on the target may also be received from building sides. Our method aims to complement the work of Di Napoli *et al.* (2020) by accounting for reflections and emissions from street canyon facets.

We verify our WBGT estimates from NWP model data against values derived from measurements of black-globe temperature, air temperature, humidity, and wind speed within street canyons. While there have been many observation campaigns using black globes, few studies have used their measurements to verify models that calculate heat stress. Thorsson *et al.* (2007) and Krüger *et al.* (2014) calculated MRT from black-globe observations and compared this with estimates from RayMan; De Lieto Vollaro *et al.* (2013) took the same approach and included SOLWEIG and ENVI-Met. The heat stress models in these studies, however, were driven by observations rather than NWP model data. In contrast, Leroyer *et al.* (2018) calculated WBGT and UTCI from MRT over the Toronto area using street-canyon fluxes determined by the Town Energy Balance model (Masson, 2000), which is coupled to the Canadian Global Environmental Multi-Scale Model. While their study does compare black-globe WBGT data with values derived from NWP output, the performance of their method is not verified in street canyons, as their urban observation sites were all situated on rooftops.

In this study, we present "UCanWBGT" ("Urban Canyon Wet-Bulb Globe Temperature"), a heat-stress model that calculates MRT analytically for an infinite street-canyon geometry and, from this, determines WBGT using empirical relationships. It is designed specifically to use standard meteorological output fields from the Met Office Unified Model, although it is general enough to be applicable to any NWP or climate model. While the principles of radiative transfer in a canyon are not new, our model formulates the MRT calculations in a novel and versatile way that allows the user to calculate WBGT over a large area, or at specific locations where the canyon geometry is known. Furthermore, we believe that this study is the first to use black-globe observations in a street canyon to validate such a model. The article is structured as follows. We present the UCanWBGT approach in Section 2, then compare our estimates of WBGT calculated from high-resolution NWP output with values calculated from black-globe temperature observations in street canyons in Paris (Section 3), made as part of the Paris Region Urban Atmospheric Observations and Models for Interdisciplinary Research (PANAME) project. In Section 4, we demonstrate a potential application of UCanWBGT by calculating WBGT along the 2024 Paris Olympics marathon route and demonstrate, by comparing calculated WBGT values with safety thresholds published in the literature, how forecasts of WBGT could be used to inform decisions on the timing of the event and indeed, potentially, the chosen route. We discuss the implications of the results in Section 5, then conclude in Section 6.

2 | THE UCANWBGT METHOD

In this section, we present the full equation set of the UCanWBGT calculation. For clarity, the improvements of UCanWBGT affect only the radiative transfer component of the WBGT calculation via the equations that are presented in Sections 2.1–2.6. UCanWBGT does not modify the temperature, humidity, or wind fields—these should be provided as in-canyon estimates from the NWP model outputs. Hence, any inaccuracies in determining these fields will be inherited in the calculated WBGT. Section 2.7 then presents the equations to calculate WBGT, then Section 2.8 concludes with the step-by-step procedure of a UCanWBGT calculation.

2.1 | Mean radiant temperature formulation

The mean radiant temperature T_{MRT} of a black globe can be written in terms of the radiative energy balance at its surface:

$$\epsilon_{\mathrm{g}}\sigma(T_{\mathrm{MRT}}+273.15)^4 = a_{\mathrm{g}}(I+K+L), \tag{1}$$

where ϵ_{g} is the longwave emissivity of the globe and a_{g} is its broadband absorptivity, and σ is the Stefan–Boltzmann constant ($5.67\times10^{-8}\,\mathrm{Wm^{-2}K^{-4}}$). In the subsequent sections, we present a set of equations that can be used to provide an estimate of the incident shortwave direct (I), shortwave diffuse (K), and longwave (L) radiation on the globe.

In UCanWBGT, the globe is situated in an infinitely long, straight canyon of width W with a continuous building on either side, both of which are of height H. The globe is located within the canyon at a height Z above the road level and horizontal distance X away from the centre line of the canyon (see Figure 1a) and can be considered negligible in size with respect to the size of the canyon. We assume that surface temperature, shortwave albedo, and longwave emissivity are constant across facets. These properties may be different between walls and road, but must be the same for both walls. Any diffuse fluxes leaving a facet, whether reflected or emitted, are assumed to be uniformly distributed across the facet (although, in the case of reflected shortwave direct radiation, not necessarily over the entire facet—see Section 2.5). We assume diffuse radiation is reflected or transmitted uniformly in all directions, and that all radiation passes unimpeded between canyon facets (in other words, interactions with air are neglected).

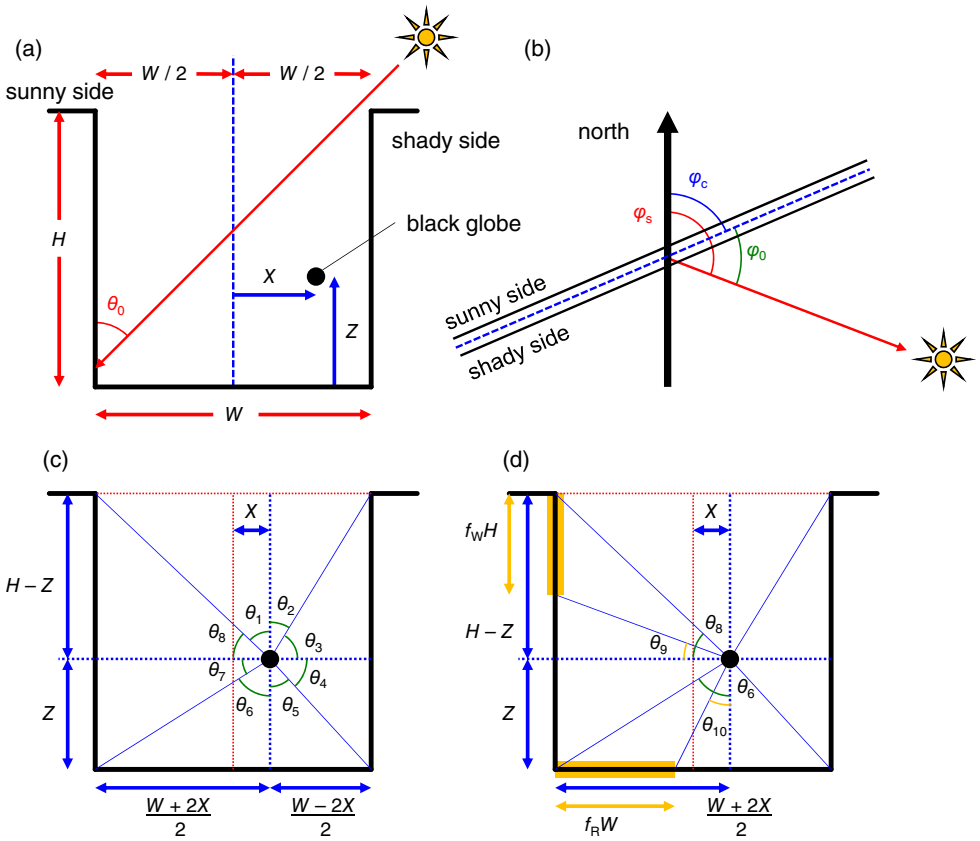

FIGURE 1 A sequence of diagrams of the canyon formulation used in UCanWBGT: (a) a cross-section through the canyon showing its geometry and how the position of the black globe is defined; (b) an overhead view to demonstrate how canyon azimuth angle ϕ_0 is determined from the canyon orientation angle ϕ_c and the solar azimuth angle ϕ_s; (c) the angles used in the calculation of viewing fractions of canyon facets from the globe; (d) the angles used for viewing fractions of partially illuminated facets, as indicated by the highlighted sections. Note that, despite its depiction in panel (d), it is not possible for both wall and road to be partially illuminated. [Colour figure can be viewed at wileyonlinelibrary.com]

2.2 | Shortwave direct flux

UCanWBGT represents a street with a particular angle with respect to the alignment of the Sun, which we term the canyon azimuth angle ϕ_0 (Figure 1b). For a canyon aligned at an angle ϕ_c from north and a solar azimuth angle ϕ_s, also defined from north, the canyon azimuth angle is defined as

$$\phi_0 = \phi_s - \phi_c. \tag{2}$$

In other words, for $\phi_0 = 0°$, the Sun shines directly along the canyon; for $\phi_0 = 90°$, it shines perpendicularly to it.

The shortwave direct radiation illuminating the globe, I, is straightforward to determine (Figure 2a). The downward direct shortwave term provided as model output is typically the vertical component $I_\downarrow$, which we can convert to the full direct flux by dividing by the cosine of the solar zenith angle, θ_0:

$$I = \frac{I_\downarrow}{4\cos(\theta_0)}. \tag{3}$$

The factor of four in the denominator is the ratio of the globe cross-section to its surface area. For a person-shaped target, this ratio (commonly referred to as f_p in the literature) has directional dependence (Jendritzky & Nübler, 1981); for a sphere, it takes a constant value of 0.25.

In the canyon, the globe may not always be illuminated by the direct beam—if the Sun is obscured behind a building, I must be set to zero. The critical angle β is the angle between the zenith and the building top in the direction of the Sun. If the Sun is located to the right in Figure 1c and the Sun shines in a perpendicular direction to the canyon, the limit is simply angle θ_2. If the Sun is at a different azimuth, a dependence on canyon azimuth angle is included:

$$\beta = \arctan\left[\frac{W - 2X}{2(H - Z)\sin(\phi_0)}\right]. \tag{4}$$

In other words, if $\theta_0 < \beta$, then I takes the value as defined by Equation (3); if $\theta_0 \geq \beta$, then $I = 0$.

Given the globe can be located anywhere in the canyon, it is important to differentiate between the "sunny" and "shady" walls in our model, in contrast to Masson (2000), Kusaka *et al.* (2001), Oleson *et al.* (2008), and Wang *et al.* (2013), who consider mean fluxes across both walls as a single value. Following Figure 1a, we set positive values of X to denote a displacement towards the shady wall and negative values to denote a displacement towards the sunny wall. For consistency, we therefore need the condition that the canyon is always illuminated from the "positive X" side (the right side in Figure 1a). This condition is met for any case where canyon azimuth angle

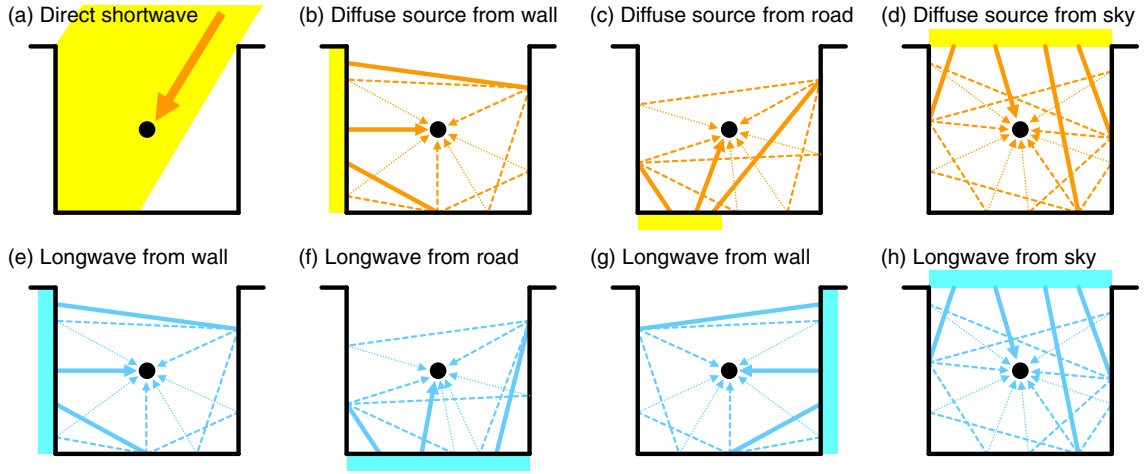

FIGURE 2 Diagrams showing the contributions to the total incident radiation that arrives at the surface of the black globe from (a) the direct shortwave, (b, c) the diffuse shortwave reflected off canyon facets, (d) the incident diffuse shortwave, (e, f, g) the longwave radiation emitted from canyon facets, and (h) the longwave radiation originating from the sky. Arrows indicate possible paths of radiation to the globe allowing up to two diffuse reflections. [Colour figure can be viewed at wileyonlinelibrary.com]

is in the range $0° < \phi_0 \leq 180°$; otherwise, the canyon would be illuminated from the "negative X" side. A simple fix to ensure mathematical consistency can be made by effectively reversing the canyon if the condition is not met: adding 180° if $-180° < \phi_0 < 0°$ or subtracting 180° if $180° \leq \phi_0 < 360°$, and translating the globe to the same displacement the other side of the canyon centre line (in other words, $X \rightarrow -X$).

2.3 | Viewing fractions

We calculate the transfer of diffuse radiation around the canyon using viewing fractions. We define the canyon as having four facets: a road at the bottom, a wall on either side, and a "sky" at the top (an imaginary facet between the tops of the two walls through which radiation may pass freely). A viewing fraction is defined as the fraction of diffuse radiation leaving one facet of the canyon that is intercepted by another. We use the viewing fractions presented by Harman *et al.* (2004). We follow their definitions exactly, noting that here we define F_{ij} as the fraction of radiation *leaving* surface i that *arrives at* surface j:

$$F_{\mathrm{sr}} = F_{\mathrm{rs}} = \left(1 + \left(\frac{H}{W}\right)^2\right)^{1/2} - \frac{H}{W}, \tag{5}$$

$$F_{\mathrm{ww}} = \left(1 + \left(\frac{W}{H}\right)^2\right)^{1/2} - \frac{W}{H}, \tag{6}$$

$$F_{\mathrm{wr}} = F_{\mathrm{ws}} = \frac{1}{2}(1 - F_{\mathrm{ww}}), \tag{7}$$

$$F_{\mathrm{rw}} = F_{\mathrm{sw}} = \frac{1}{2}(1 - F_{\mathrm{sr}}). \tag{8}$$

Subscripts "r", "w", and "s" refer to road, wall, and sky, respectively.

We also need a second set of viewing fractions to determine the amount of diffuse radiation that falls on the globe from each facet. As the globe is spherical, it receives radiation equally from all directions—hence the total incident diffuse radiation can be calculated as a mean flux across all facets weighted by the solid angle they subtend from the globe. Furthermore, as the canyon is infinitely long and straight, the solid angles of the facets from the globe are proportional to the two-dimensional angles of the facets to the globe in a cross-section through the canyon. This implies that the viewing fractions may be defined simply in terms of two-dimensional geometry (Figure 1c). For example, the sky viewing fraction is $(\theta_1 + \theta_2)/2\pi$, the road viewing fraction is $(\theta_5 + \theta_6)/2\pi$, and so on. Expanding these angles in terms of the canyon geometry gives the following:

$$F_{\mathrm{s}} = \frac{1}{2\pi}\left(\arctan\left(\frac{W + 2X}{2(H - Z)}\right) + \arctan\left(\frac{W - 2X}{2(H - Z)}\right)\right), \tag{9}$$

$$F_{\mathrm{r}} = \frac{1}{2\pi}\left(\arctan\left(\frac{W - 2X}{2Z}\right) + \arctan\left(\frac{W + 2X}{2Z}\right)\right), \tag{10}$$

$$F_{\mathrm{w1}} = \frac{1}{2\pi}\left(\arctan\left(\frac{2Z}{W + 2X}\right) + \arctan\left(\frac{2(H - Z)}{W + 2X}\right)\right), \tag{11}$$

$$F_{\mathrm{w2}} = \frac{1}{2\pi}\left(\arctan\left(\frac{2(H - Z)}{W - 2X}\right) + \arctan\left(\frac{2Z}{W - 2X}\right)\right), \tag{12}$$

$$F_{\mathrm{w}} = F_{\mathrm{w1}} + F_{\mathrm{w2}}. \tag{13}$$

Here, F_s and F_r are the viewing fractions of the sky and road from the globe, respectively; F_{w1} is the viewing fraction of the sunny wall, F_{w2} is the viewing fraction of the shaded wall, and F_w is the total viewing fraction of *both* walls.

2.4 | Shortwave diffuse flux from the sky

Shortwave diffuse radiation is distributed around the canyon using viewing fractions and shortwave albedo. We partition the shortwave diffuse radiation received by the globe (K) into three components based on the facet from which it *originates*:

$$K = K_s + K_r + K_w. \tag{14}$$

The first term K_s refers to diffuse radiation received by the globe that originated from the downward diffuse radiation from the sky, which can be taken as the model output value of downward shortwave diffuse flux, $K_\downarrow$. A fraction of this flux is incident on the globe; the remainder can be reflected around the canyon using the Harman *et al.* (2004) viewing fractions. In our model, we permit only two reflections, following the approaches of Kusaka *et al.* (2001) and Wang *et al.* (2013) (noting that the former study refers to the approach as one reflection; here, the second reflection accounts for reflection off facets and on to the globe). This approximation results in radiation from higher order reflections being lost, although we will later demonstrate in Section 3 that it is a fair approximation for a realistic range of building materials. If we write out a full list of paths that diffuse radiation originating from the sky can take on its way to the globe with zero, one, or two reflections (ignoring any radiation that exits the canyon to the sky; see Figure 2d), we end up with the following equation:

$$\frac{K_s}{K_\downarrow} = F_s + (F_{sr}\alpha_r + 2F_{sw}F_{wr}\alpha_w\alpha_r)F_r + (F_{sw}\alpha_w + F_{sw}F_{ww}\alpha_w^2 + F_{sr}F_{rw}\alpha_r\alpha_w)F_w. \tag{15}$$

Masson (2000) accounts for infinite shortwave diffuse reflections between road and walls in his model by presenting total fluxes as a sum over an infinite geometric series. However, his approach considers reflections between walls and road using symmetrical arguments, assuming average illumination over both walls. Given the need for us to keep a distinction between sunny and shady walls, expressing the multitude of possible paths in terms of a geometric series is much less trivial.

2.5 | Shortwave diffuse flux from the road and walls

The K_r and K_w in Equation (14) refer to the diffuse shortwave flux originating from the road and sunny wall, respectively. These terms arise from the diffuse reflection of direct solar radiation. Given the assumption that diffuse reflected radiation is uniformly distributed in all directions, we can consider the illuminated regions of the wall and road to be shortwave diffuse sources with outgoing fluxes, defined as

$$S_r = I_\downarrow \alpha_r, \tag{16}$$

$$S_w = I_\downarrow \alpha_w \tan(\theta_0)\sin(\phi_0). \tag{17}$$

The diffuse source out of the road is simply the downward component of the direct beam multiplied by the albedo of the road. The diffuse source on the wall is the component of the direct beam that is incident on the wall, hence it is dependent on both the solar zenith and canyon azimuth angles.

Diffuse radiation from the road and the sunny wall can then be treated in a similar way to that entering from the sky. However, the diffuse source may not be distributed across the whole of the two facets, as the building on the shady side of the canyon will cast a shadow. We define the illuminated fraction of the wall and road to be f_w and f_r, respectively, and, given the behaviour of the Sun in a canyon with varying Sun position, partial illumination of the sunny wall with increasing f_w is downward from the canyon top and partial illumination of the road with increasing f_r is from the base of the sunny wall across towards the base of the shady wall. The illuminated fractions can be derived from canyon geometry:

$$f_r = 1 - \frac{H\tan(\theta_0)\sin(\phi_0)}{W}, \tag{18}$$

$$f_w = \frac{W}{H\tan(\theta_0)\sin(\phi_0)}. \tag{19}$$

If we are in the "partial wall" regime (where the shadow extends part of the way up the wall; $0 \le f_w \le 1$ and $f_r < 0$ according to the above equations), then f_w should take its value from Equation (18), while f_r should be fixed to zero, as the entire road must be shaded. If we are in the "partial road" regime (where the shadow extends part of the way across the road; $0 \le f_r \le 1$ and $f_w > 1$), then f_r should take its value from Equation (19), while f_w should be fixed to one, as the entire sunny wall must be illuminated.

To handle the distribution of diffuse radiation from partially illuminated canyon facets to other facets, we require a new set of "partial" viewing fractions. These

can be calculated following the approach of Harman *et al.* (2004). We extend the viewing fractions presented in configurations #14 and #15 from appendix A of Sparrow and Cess (1978) to apply for infinitely long street canyons to give the following partial viewing fractions:

$$F_{prw1} = \frac{1}{2} + \frac{H - \sqrt{H^2 + f_r^2 W^2}}{2 f_r W}, \tag{20}$$

$$F_{prw2} = \frac{1}{2} + \frac{\sqrt{H^2 + (1-f_r)^2 W^2} - \sqrt{H^2 + W^2}}{2 f_r W}, \tag{21}$$

$$F_{prs} = \frac{\sqrt{H^2 + f_r^2 W^2} - \sqrt{H^2 + (1-f_r)^2 W^2} + \sqrt{H^2 + W^2} - H}{2 f_r W}, \tag{22}$$

$$F_{pw1r} = \frac{1}{2} + \frac{\sqrt{W^2 + (1-f_w)^2 H^2} - \sqrt{W^2 + H^2}}{2 f_w H}, \tag{23}$$

$$F_{pw1w2} = \frac{\sqrt{W^2 + f_w^2 H^2} - \sqrt{W^2 + (1-f_w)^2 H^2} + \sqrt{W^2 + H^2} - W}{2 f_w H}, \tag{24}$$

$$F_{pw1s} = \frac{1}{2} + \frac{W - \sqrt{W^2 + f_w^2 H^2}}{2 f_w H}. \tag{25}$$

It can be shown that these equations give the "full" viewing fractions of Harman *et al.* (2004) for $f_r = f_w = 1$ (Equations 5–8). Note also that we have only presented these equations in terms of viewing fractions leaving the road and the sunny wall, as these are the only facets that may be illuminated by the Sun.

The viewing fractions of the partially illuminated surfaces from the globe can be determined again by geometry in a two-dimensional cross-section through the canyon (Figure 1d)—the partial viewing fraction of the wall is $(\theta_8 - \theta_9)/2\pi$ and the partial viewing fraction of the road is $(\theta_6 - \theta_{10})/2\pi$:

$$F_{pr} = \frac{1}{2\pi}\left(\arctan\left[\frac{W + 2X}{2Z}\right] - \arctan\left[\frac{(1-2f_r)W + 2X}{2Z}\right]\right), \tag{26}$$

$$F_{pw1} = \frac{1}{2\pi}\left(\arctan\left[\frac{2(H-Z)}{W + 2X}\right] - \arctan\left[\frac{2((1-f_w)H - Z)}{W + 2X}\right]\right). \tag{27}$$

Again, from a list of the possible paths taken by radiation leaving the illuminated wall and road surfaces, using the viewing fractions presented throughout this section and allowing for two reflections (see Figure 2b,c), the incident radiation on the globe is given by

$$\frac{K_r}{S_r} = F_{pr} + \left(F_{prw1}\alpha_w + F_{prw2}\alpha_w^2 F_{ww}\right)F_{w1} + \left(F_{prw2}\alpha_w + F_{prw1}\alpha_w^2 F_{ww}\right)F_{w2} + \left(F_{prw1}\alpha_w F_{wr}\alpha_r + F_{prw2}\alpha_w F_{wr}\alpha_r\right)F_r, \tag{28}$$

$$\frac{K_w}{S_w} = F_{pw1} + \left(F_{pw1r}\alpha_r + F_{pw1w2}\alpha_w F_{wr}\alpha_r\right)F_r + \left(F_{pw1w2}\alpha_w + F_{pw1r}\alpha_r F_{rw}\alpha_w\right)F_{w2} + \left(F_{pw1r}\alpha_r F_{rw}\alpha_w + F_{pw1w2}\alpha_w^2 F_{ww}\right)F_{w1}. \tag{29}$$

Note that, following the first reflection of the direct beam off part of either the road or the sunny wall, subsequent reflections assume reflected radiation to be evenly distributed over whole facets. Note also that our terminology "two reflections" here means that two reflections of the diffuse shortwave are permitted—technically, this implies that three reflections of the direct radiation are permitted, as the transfer from direct beam to diffuse source could be considered a first reflection.

2.6 | Longwave flux

As longwave emission from all facets (and indeed through the sky) is considered to be diffuse, we can adapt the equations for the shortwave diffuse radiative transfer to describe the longwave transfer within the canyon. We use the same viewing fractions and again limit the number of reflections to two, following Masson (2000), Kusaka *et al.* (2001), and Wang *et al.* (2013). The error associated with this assumption has been shown to be small for surfaces with typical emissivity values of buildings (Harman *et al.*, 2004; Johnson *et al.*, 1991).

As for shortwave diffuse radiation, we partition the longwave radiation incident on the globe (L) into three components:

$$L = L_s + L_r + L_w, \tag{30}$$

where the three terms on the right represent the longwave flux on the globe that originates from downward flux from the sky, emission from the road, and emission from *both* walls, respectively.

The longwave radiation entering through the sky behaves identically to the shortwave diffuse radiation (Figure 2h). The component of this that illuminates the globe is therefore an adapted version of Equation (15):

$$\frac{L_s}{L_\downarrow} = F_s + (F_{sr}\eta_r + 2F_{sw}F_{wr}\eta_w\eta_r)F_r + \left(F_{sw}\eta_w + F_{sw}F_{ww}\eta_w^2 + F_{sr}F_{rw}\eta_r\eta_w\right)F_w. \tag{31}$$

Note that we have used η as the symbol for longwave reflectivity to avoid confusion with earlier notation; for a surface i, this is given by $\eta_i = 1 - \epsilon_i$.

Longwave radiation emitted from the road is simply the emission according to the Stefan–Boltzmann equation. This is equivalent to the shortwave diffuse sources, but with emission over the whole surface (Figure 2f). We can therefore modify Equation (28) by replacing the shortwave source with the longwave emission, replacing shortwave albedo with longwave reflectivity and setting $f_r = 1$:

$$\frac{L_r}{\epsilon_r \sigma T_r^4} = F_r + \left(F_{rw}\eta_w + F_{rw}\eta_r^2 F_{ww}\right)F_w + 2F_{rw}\eta_w F_{wr}\eta_r F_r. \tag{32}$$

Equation (29) can be adapted in a similar way to distribute the longwave radiation emitted by the sunny wall (that is, setting $f_w = 1$). However, we must also add extra terms to account for longwave emission from the shady wall (Figure 2e,g). Writing out the paths for both walls and combining them into a single equation results in

$$\frac{L_w}{\epsilon_w \sigma T_w^4} = F_w + 2(F_{wr}\eta_r + F_{ww}\eta_w F_{wr}\eta_r)F_r + \left(F_{ww}\eta_w + 2F_{wr}\eta_r F_{rw}\eta_w + F_{ww}^2\eta_w^2\right)F_w. \tag{33}$$

2.7 | Wet-bulb globe temperature formulation

From the equations in the previous subsections, we can calculate the radiative components incident on the globe and obtain the MRT by rearranging Equation (1). The MRT can then be used as an input to the WBGT calculation. The original version of the WBGT equation is given by (Parsons, 2006)

$$T_{WBGT} = 0.7T_{wb} + 0.3(a_h a_g(T_g - T) + T), \tag{34}$$

where T_{wb} is the wet-bulb temperature, T_g is the black-globe temperature, T is the air temperature, a_h is the absorptivity of a human, and a_g is the absorptivity of a black-globe thermometer (taken here to be 0.95; Parsons, 2006). All temperature quantities in the equation are in °C. The standard a_h values for a clothed standing human are 0.97 for longwave radiation (a_{LW}) and 0.7 for shortwave radiation (a_{SW}) (Leroyer *et al.*, 2018). Substituting a_{SW} and a_g values into Equation (34) gives, to a good approximation,

$$T_{WBGT} = 0.7T_{wb} + 0.2T_g + 0.1T, \tag{35}$$

which is the ISO 7243 standard equation for outdoor environments when illuminated by the Sun (ISO 7243, 1989). In shady conditions, it can generally be assumed that longwave radiation dominates shortwave radiation, so that $a_h = a_{LW}$. Substituting the a_{LW} value into Equation (34), to a good approximation one obtains

$$T_{WBGT} = 0.7T_{wb} + 0.3T_g, \tag{36}$$

which is the ISO 7243 standard equation for outdoor environments shaded from the Sun (ISO 7243, 1989; Leroyer *et al.*, 2018). The approximation in Equation (36) is that a_g and a_{LW} equal one, so that the clothed human and black globe are perfect absorbers of longwave radiation.

We use Equation (34) rather than the two separate ISO standard equations so that the WBGT is consistent whether the calculation is in sunny or shady conditions, and no approximations with coefficients need to be made. Furthermore, as longwave and shortwave radiation are both likely to be significant in a canyon, instead of fixing a_h to either a_{SW} or a_{LW} (as is often done in the literature), we take a simple linear combination weighted by the shortwave fraction $r = (I + K)/(I + K + L)$, so that

$$a_h = (1 - r)a_{LW} + ra_{SW}, \tag{37}$$

where I, K, and L are the shortwave direct, shortwave diffuse, and longwave fluxes illuminating the globe as determined from the MRT calculation.

Black-globe temperature T_g is calculated by calculating the energy balance at the surface of the black-globe thermometer. This accounts for both radiation balance and sensible heat transfer from the globe and can be expressed as (Leroyer *et al.*, 2018)

$$\epsilon_g \sigma (T_{MRT} + 273.15)^4 = \epsilon_g \sigma (T_g + 273.15)^4 + h_{cg}(T_g - T), \tag{38}$$

where ϵ_g is the emissivity of the surface of the black-globe thermometer (assumed equal to a_g) and h_{cg} is the convective coefficient for heat transfer between the globe and the air for forced convection, required for outdoor calculations. The first and second terms on the right-hand side account for the longwave radiative flux emitted and sensible heat flux from the surface of the globe, respectively. The formulation of h_{cg} employed here follows ISO 7726 (1998):

$$h_{cg} = 6.3\frac{U^{0.6}}{d^{0.4}}, \tag{39}$$

where U is the wind speed and d is the diameter of the black-globe thermometer sphere, taken to be the standard 0.15 m. The analytical solution for T_g from Equations (38) and (39) is detailed below (and follows Leroyer *et al.*, 2018, appendix A). Equation (38) can be rewritten as

$$(T_g + 273.15)^4 + a(T_g + 273.15) - b = 0, \quad (40)$$

where

$$a = \frac{h_{cg}}{\epsilon_g \sigma}; \quad b = (T_{MRT} + 273.15)^4 + a(T + 273.15).$$

This has the solution

$$T_g = i - j - 273.15, \quad (41)$$

where

$$i = 0.5\left(\frac{2a}{\sqrt{k}} - k\right)^{0.5};$$
$$j = \frac{\sqrt{k}}{2}; \qquad k = 0.381571E - \frac{Q}{E};$$
$$Q = 3.4943\, b; \qquad E = (m + 1.73205\sqrt{n + p})^{1/3};$$
$$m = 9a^2; \qquad n = 27a^4; \qquad p = 256b^3. \quad (42)$$

This formulation of h_{cg} is applicable for ventilated cases; that is, where $U > 0.15\,\mathrm{m \cdot s^{-1}}$. For very low wind speeds, this equation produces unphysically low values of T_g. Hence, we set $0.15\,\mathrm{m \cdot s^{-1}}$ as the minimum permitted wind speed; any speeds below this are set to $0.15\,\mathrm{m \cdot s^{-1}}$.

2.8 | Procedure to calculate WBGT

The UCanWBGT calculation procedure follows Figure 3 and consists of four steps:

(1) calculate wet-bulb temperature T_{wb} from air temperature, humidity, and surface pressure;
(2) calculate the incident fluxes on the globe (I, K, and L) from the downward fluxes, surface temperatures, canyon geometry, and surface optical properties, then apply them to determine mean radiant temperature T_{MRT} using Equation (1);
(3) calculate black-globe temperature T_g using mean radiant temperature and wind speed;
(4) calculate wet-bulb globe temperature by substituting T, T_{wb}, and T_g into Equation (34).

Wet-bulb temperature can be determined either adiabatically (by raising a parcel of air adiabatically until it reaches saturation, then lowering it to its original pressure) or isobarically (by evaporating water into a parcel of air at constant pressure until it reaches saturation). While these two versions of wet-bulb temperature give slightly different values, both approaches are appropriate for studies of heat extremes (Warren, 2025). However, the standard

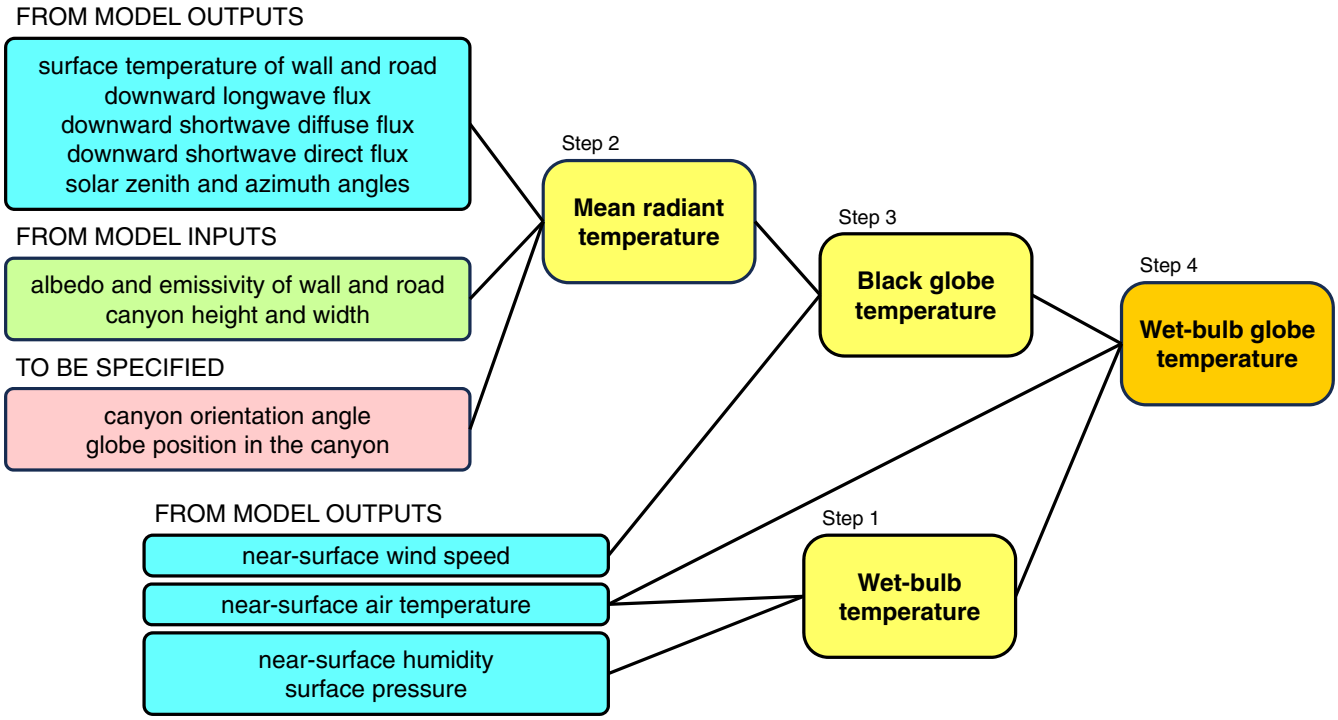

FIGURE 3 Schematic of the UCanWBGT calculation. A list of required input variables in presented in the boxes to the left. The lines then indicate which variables are used in the calculation of the three temperature terms used in the final WBGT calculation. Step numbers follow those marked in the list at the beginning of Section 2.8. [Colour figure can be viewed at wileyonlinelibrary.com]

wet-bulb temperature formulation for a WBGT calculation is the isobaric wet-bulb temperature (Parsons, 2006, who refer to it as "natural" wet-bulb temperature). We calculate isobaric wet-bulb temperature using the method in the Python library introduced by Warren (2025).

The leftmost boxes in Figure 3 list the input variables required for a WBGT calculation using UCanWBGT. Of these, all but three (height and horizontal position of black globe, and canyon orientation angle) can typically be extracted from either model output or model input surface properties. In the interests of versatility, we leave the choice of how to define these three variables to the user, depending on their desired application. If the aim is to calculate WBGT at specific locations within an NWP domain in which the canyon orientation angle is known or can be measured (for example, to forecast the heat stress on people at certain locations in a particular street), these values can be specified directly, with the globe location set to a typical height of a person (say, $Z = 1.5$ m). Furthermore, if the building height and canyon width are also known, these values may be substituted in place of the model geometry, with the WBGT calculation only taking meteorological and radiative fields from the NWP model output. This approach is also applicable for comparison studies with black-globe observations in a canyon where the geometry and globe position are known (as in Section 3 of this study).

If the aim is to use UCanWBGT within an NWP model to calculate WBGT over a large area using the surface geometry provided to the model, then the globe position and the canyon orientation angle are unlikely to be known values. When handling surface transfer in an NWP model, the standard approach is to consider street canyons as randomly aligned in orientation. Such generalisation allows for simplifications of the radiative transfer calculation and the lack of distinction between sunny and shady walls (Masson, 2000; Porson *et al.*, 2010), and the possibility of treating the shortwave transfer in terms of infinite reflections (Masson, 2000). However, for reasons previously stated, extending our approach in this way is not straightforward. We propose that, when using UCanWBGT for this application, a small number of WBGT calculations be performed that span all canyon orientation angles from $0° < \phi_0 \leq 90°$ and all globe positions across the canyon. We recognise that this approach introduces an element of numerical integration, which we specifically stated in Section 1 that we wanted to avoid. However, the increase in computation time is offset by the efficiency of UCanWBGT given its reliance on analytical and empirical equations. We found that running UCanWBGT for three angles (15°, 45°, and 75°) and five globe positions, evenly spaced across the canyon, provides a generally unbiased estimate of the WBGT with respect to a similar calculation over a large number of angles and positions, and a root-mean-square error of order 0.1 °C, for the data over the Paris area presented in Section 4 of this study.

3 | VERIFICATION AGAINST PARIS OBSERVATIONS

In this first results section, we compare WBGT values calculated using UCanWBGT from high-resolution model simulation data with WBGT derived from measurements of black-globe temperature made on location in the streets of Paris.

3.1 | Paris black-globe data

We use data from a network of sensors deployed across and around Paris as part of the PANAME project (Lemonsu *et al.*, 2025; https://paname.aeris-data.fr/). Nine sites in Paris were selected and fitted with black-globe thermometers and sensors to detect air temperature, humidity, and wind speed. Six of the nine sites are used this study. The location, canyon morphology, and globe position at the sites are listed in Table 1; Figure 4 shows maps of the area around each site and how the canyon morphology is determined. Three of the sites are situated in straight, city-centre street canyons with tall buildings either side (typical heights 20–25 m). Rue de Rivoli (RDR: Figure 4a) is a main road with no trees; Boulevard St Germain (BSG: Figure 4b) is a wide tree-lined boulevard; Rue Jacques Callot (RJC: Figure 4c) is a much narrower side street. Another three sites are situated in more complex urban geometries. Avenue Maréchal Galieni Invalides (AMGI: Figure 4d) is a very wide avenue with a road flanked by grass and rows of trees with buildings beyond; Place Vendôme (PV: Figure 4e) is a paved square surrounded by tall buildings; Quai Anatole France (QAF: Figure 4f) is a walkway along the side of the River Seine with walls either side of the river. These sites can be included in our study by approximating the sites to be canyons: at AMGI, we take the distance between the buildings to define the canyon width; at PV, we consider the canyon width to be the width of the square (parallel to the streets into and out of the square at each end). At both sites, we define the canyon height to be the height of the surrounding buildings. At QAF, we model the canyon width to span the river and consider the walls on either side to be the canyon walls. While the geometry of these sites may lie outside a typical urban canyon regime, we include them in this study to examine the performance of the model over as wide a range of geometries as possible. The remaining three sites are located in parks and not considered in this study.

TABLE 1 Information, location, and estimated canyon morphology at the six urban sites that are considered in this study. The coordinates indicate the location of the black-globe thermometers.

Site name (abbreviation)	Lat/°	Long/°	H/m	W/m	ϕ_c/°	Z/m	X/m
Rue de Rivoli (RDR)	48.85926	2.34612	24	20	116	3	−6
Boulevard St Germain (BSG)	48.85397	2.33296	24	38	109	3	−12
Rue Jacques Callot (RJC)	48.85531	2.33722	22	10	090	3	−2
Avenue Maréchal Galieni Invalides (AMGI)	48.85990	2.31251	20	260	004	3	−43
Place Vendôme (PV)	48.86752	2.32978	24	120	033	3	+18
Quai Anatole France (QAF)	48.86135	2.32358	18	160	115	3	+73

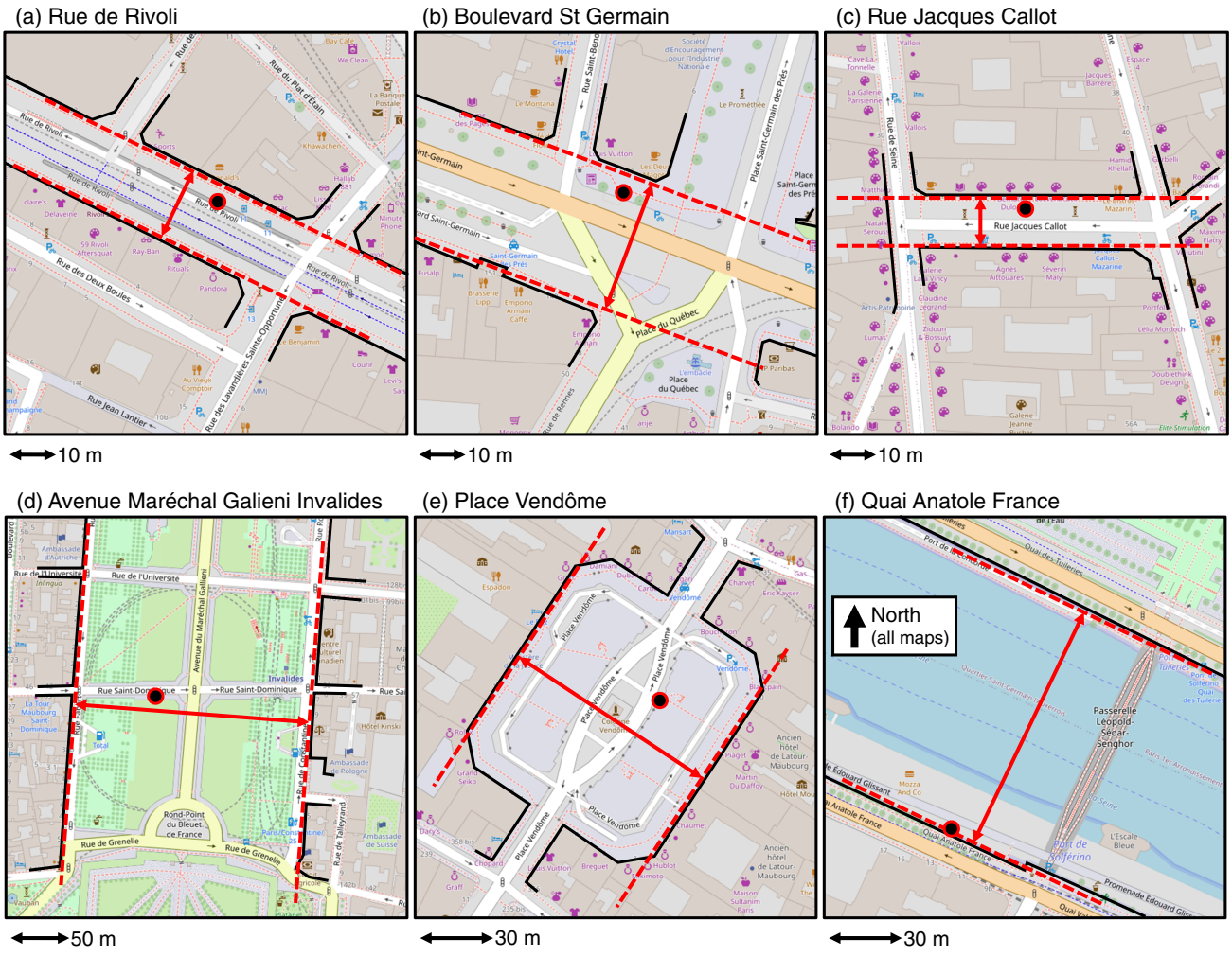

FIGURE 4 Maps of the areas surrounding the six sites used in this study. Building edges around each site have been highlighted in solid black lines (except at QAF, where black lines indicate the walls surrounding the river and walkways). Dashed lines indicate how each site is modelled as a street canyon. The location of the globe at each site is indicated by the circle. Scales for each map are indicated beneath; note that the scales are different across panels. Map data: © OpenStreetMap. [Colour figure can be viewed at wileyonlinelibrary.com]

The black globes are attached to lamp posts at locations given by the longitude and latitude coordinates in Table 1. They are mounted on arms on the south side of the lamp posts to avoid a shadow being cast on the globe. Furthermore, the lamp posts are all painted in dark colours, so diffuse shortwave reflections are limited and are likely to be similar enough in temperature to the surroundings not to impact the longwave budget massively. The meteorological sensors that measure temperature, humidity, and wind speed are installed on different lamp posts on

the same street as the black globes, and all but one are within a distance of 75 m (more than half of them are within 40 m). This presents a potential source of inconsistency in the WBGT calculation between radiation and meteorological measurements. For the purpose of this study, we will assume this inconsistency to be negligible. Table 1 also presents estimates of the geometry at each site. The canyon height (H), width (W), and orientation angle (ϕ_c) and horizontal globe position in the canyon (X) at the sites were estimated from measurements in Google Earth. Horizontal distances were measured by drawing paths; building height was determined by comparing the building rooftop elevation height with street-level elevation. All black globes are mounted 3 m above street level.

We select September 7, 2023 as our case-study day. This was chosen from a clear-sky heatwave period spanning September 2–10, 2023, during which the PANAME sensors were deployed. From radiometric data from PANAME sites around the edge of Paris, we calculated total insolation time at each site for each day in the period and found that, on average, September 7 was the sunniest day. Across the six urban sites, air temperature rose from an overnight minimum of about 21 °C at sunrise to maximum values of between 32 °C and 34 °C in the early afternoon. Winds were light throughout the day, with speeds mostly below $1.5\,\mathrm{m}\cdot\mathrm{s}^{-1}$.

Values of WBGT may be calculated directly from the data recorded at the black-globe thermometer sites. Air temperature and humidity are combined to calculate wet-bulb temperature via the isobaric method of Warren (2025). This can be used alongside the measured wind speed and black-globe temperature to calculate WBGT from Equation (34) without the need for an MRT calculation.

3.2 | High-resolution model simulation

For model simulations, we use a nest of high-resolution models centred on Paris, with resolutions of 1.5 km, 333 m, and 100 m. The atmosphere model is the Met Office Unified Model (UM), using the RAL3 (Regional Atmosphere and Land version 3) configuration (Bush *et al.*, 2025). The atmosphere is coupled to the Joint UK Land Environment Simulator (JULES) land-surface model (Best *et al.*, 2011; Clark *et al.*, 2011), which divides the land surface into nine tiles. We use the Met Office Reading Urban Surface Exchange Scheme (MORUSES) urban surface scheme (Porson *et al.*, 2010), which separately represents the urban surface as a rooftop tile and a canyon tile. The urban morphology information required by MORUSES (mean building height, canyon height to width ratio, and canyon width ratio) for Paris is derived from the Modélisation Appliquée et Droit de l'Urbanisme: Climat Urbain et Énergie (MApUCE) geoprocessing framework (Bocher *et al.*, 2018). The surface tile fractions are computed from the European Space Agency (ESA) Climate Change Initiative version 1 (CCIv1) land-use–land-cover (LULC) data (Bontemps *et al.*, 2013). However, at grid points where the CCIv1 identifies an urban tile, the surface tile fractions are replaced with that computed from the ESA's WorldCover v100 LULC data (Zanaga *et al.*, 2021), as WorldCover is found to give a better representation of urban areas.

The model is run for a 48-hour period, starting at 1200 UTC on the previous day (September 6, 2023) to allow the model to spin up, therefore a forecast is produced that includes the entirety of the case-study day. Using UCanWBGT, we calculate WBGT for each of the six sites from model output at the nearest grid point in the highest resolution (100 m) model. UCanWBGT uses the downward radiative fluxes at the bottom atmospheric level for the MRT calculation. Surface temperature is available on tiles in the model output, so we are able to select the surface temperature specifically on the urban canyon tile (note that only one value is stored, with walls and road being assigned the same value). Solar zenith and azimuth angles are calculated by the model from longitude, latitude, date, and time. For meteorological properties in the canyon, no tiled variables are available, so we use the best representation of these properties, which is the 1.5 m temperature, humidity, and wind speed, presented as grid-box-mean values. These are seen to compare well with observed values at the six locations (Figure 5a–c), with model temperatures during the day generally within 2 °C of observed values and model wind generally lighter.

Surface pressure can also be extracted from the model. We use the shortwave albedo and longwave emissivity values specified in the RAL3 configuration: $\alpha_w = 0.375$, $\alpha_r = 0.08$, $\epsilon_w = 0.875$, $\epsilon_r = 0.95$. For canyon geometry, we use the best estimates at the specific locations, as stated in Table 1. Values of building height and canyon width are available in the model input data, but these are representative values for individual grid boxes and do not necessarily reflect the true canyon geometry. If used, they would potentially introduce a source of error that is not of interest to this study.

3.3 | Model versus observation comparison

Figure 6 compares the WBGT calculated from the Paris observations with values derived from the NWP model data using UCanWBGT. The diurnal cycle of WBGT

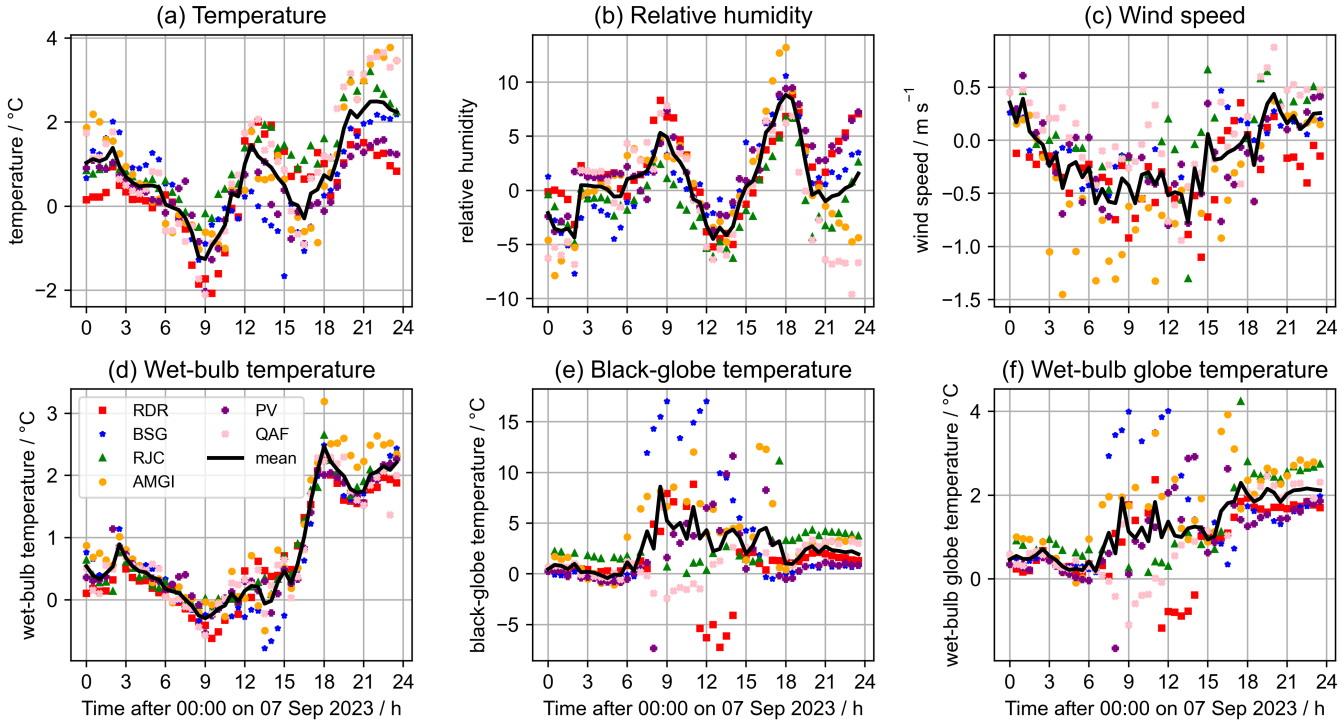

FIGURE 5 Model errors (model minus observations) in various quantities relating to the WBGT calculation at the six Paris sites. The black line indicates the mean across the sites; the markers show errors at individual sites (see legend; site abbreviations are presented in Table 1). The model MRT calculation used meteorology and radiation fields from the NWP data and best-estimate canyon geometry. [Colour figure can be viewed at wileyonlinelibrary.com]

throughout the day is well captured across the six sites, with lowest WBGT values around sunrise (0515 UTC in Paris on this day), rising through the morning to peak in the early afternoon before falling again towards sunset (1821 UTC). Steps in WBGT are seen in both model and observed data—these are caused by transitions between the globe being directly illuminated by the Sun and in the shade (for example, in the NWP data, the globe is illuminated from 0700 to 1600 at BSG and from 0800 to 1100 at RDR). At some sites, the timings of the illumination periods are generally well captured, indicating that our best estimates of canyon geometry and orientation are realistic, hence buildings are shading the globe from the Sun at or near the observed times. Timing differences at the other sites can be explained by the limitations of applying an infinite street-canyon geometry approximation to real-world canyons. The longer period of illumination in observations at RDR is associated with the Sun shining out of a side street (a gap in the canyon; see map in Figure 4a); the lack of observed illumination through the morning at BSG and late in the afternoon at AMGI is caused by sheltering from trees. The short periods of erroneous illumination in the NWP data at RJC at each end of the day are a result of the infinitely long canyon approximation—in observations, this illumination is blocked by buildings at the ends of the street (see Figure 4c).

There are WBGT errors common to all sites—in particular, values are too high both overnight and during the day when the globe is illuminated by the Sun (Figure 5f). We can attribute some of these errors to inherited errors from the model meteorological fields. Table 2 presents a summary of the mean errors in WBGT and its components, averaged across all six sites and various parts of the 24-hour period. Overnight, the consistent warm WBGT error across all fields can be attributed to the wet-bulb temperature being too high by about 2 °C (Figure 5d). Around sunset, this error is driven by a moist error in humidity (Figure 5b), although later a warm temperature error dominates (Figure 5a). There is also a contribution to error from the black-globe temperature term, also of order 2 °C or similar magnitude, although the wet-bulb temperature error dominates the WBGT error on account of its higher weighting in the WBGT equation (see Equation 34).

In the daytime, temperature and humidity errors are still noted, although their signs tend to oppose each other and hence their combined influence on wet-bulb temperature is small, with errors of magnitude less than 1 °C during the daytime (Figure 5d). Errors here are dominated by the black-globe temperature term (Figure 5e). The large scatter of points at individual sites is associated with errors between shading and illumination. Overall, there is a positive mean error across

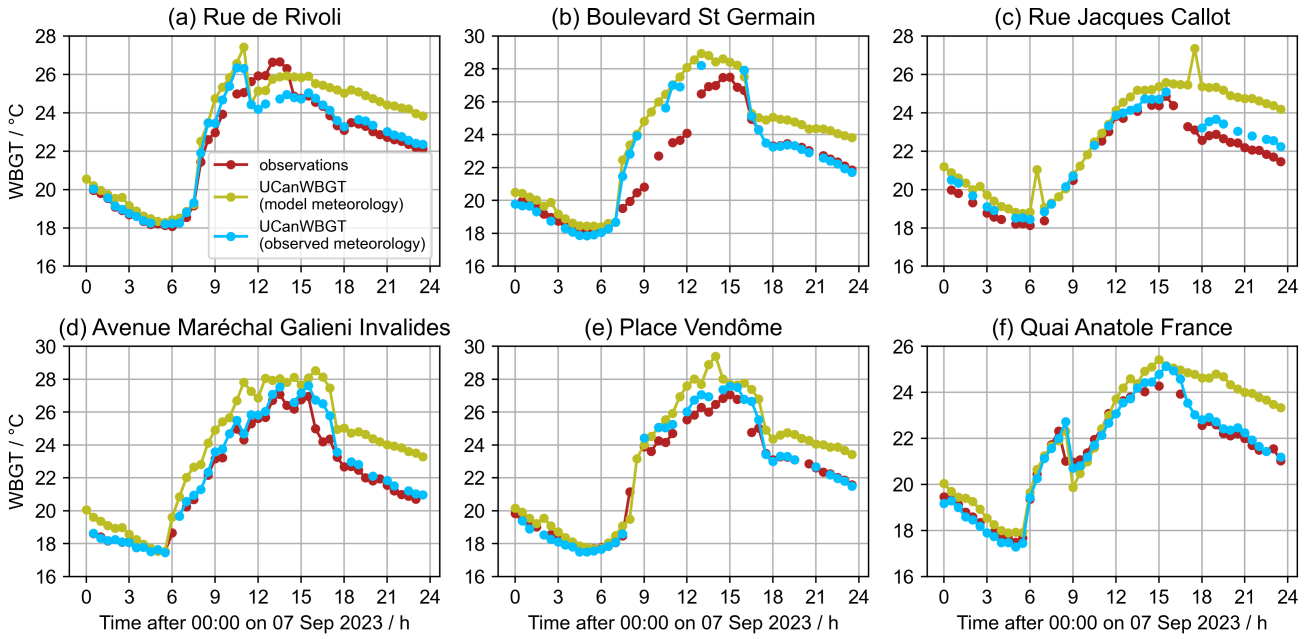

FIGURE 6 Time series of WBGT from the six sites, comparing values derived from observations and calculations from UCanWBGT using the high-resolution NWP model data. Two sets of UCanWBGT calculations are presented: one uses meteorological fields (temperature, humidity, and wind speed) from the NWP data; the other uses meteorological fields from the Paris observations. Both sets use radiation fields from NWP data and best estimates of canyon geometry and black-globe location. [Colour figure can be viewed at wileyonlinelibrary.com]

TABLE 2 Summary analysis of differences between WBGT values derived from NWP output and observations. Mean errors are calculated across the six sites and all times of the day, as listed at the top of each column. The number after the "±" symbol is the standard deviation of the errors across the sites and the time period. The top block shows error summaries for the model calculations with model meteorology; the bottom block shows the same for the calculations with observed meteorology.

	All day 0000–0000	**Morning** 0000–0600	**Daytime** 0600–1800	**Nighttime** 1800–0000
With model meteorology				
Wet-bulb globe temperature error (°C)	1.001 ± 1.413	0.423 ± 0.267	1.189 ± 1.224	2.039 ± 0.449
Black-globe temperature error (°C)	1.292 ± 4.521	0.259 ± 0.843	3.647 ± 5.073	2.007 ± 1.322
Wet-bulb temperature error (°C)	0.763 ± 0.885	0.493 ± 0.235	0.257 ± 0.606	2.047 ± 0.336
With observed meteorology				
Wet-bulb globe temperature error (°C)	0.246 ± 0.676	−0.063 ± 0.216	0.435 ± 0.901	0.218 ± 0.280
Black-globe temperature error (°C)	0.782 ± 2.731	−0.228 ± 0.780	1.341 ± 3.747	0.788 ± 1.012

sites of 3.6 °C throughout the day that is reflected in a WBGT error of slightly over 1 °C. An important influence in this error is the lower wind speed throughout the day (Figure 5c), although radiative errors are also important.

To investigate this further, a second set of UCanWBGT calculations is performed, in which the radiative flux terms are taken from the NWP output but the meteorology (temperature, humidity, and wind speed) is taken from the observed values. This implies that all WBGT errors associated with errors in the model meteorology are removed, so all remaining errors are associated with the radiative transfer. With the observed meteorology, all errors in wet-bulb temperature are removed, hence the overnight warm WBGT errors are much reduced at all sites (Figure 6), with a mean error of about 0.2 °C. The daytime warm errors are reduced from 1.2 °C to 0.4 °C but not eliminated entirely, implying that the low wind speeds in the model provide a contribution to the error, but are not the sole cause. Any remaining errors are solely due to

errors in radiation: possible sources of error include a misrepresentation of the optical properties of the walls and road in the model values, or indeed errors in the downward radiative fluxes from the model, which we are unable to compare at the Paris sites, as these are not observed.

3.4 | Sensitivity analysis

We now perform tests to investigate how the UCan-WBGT calculations from NWP model data would vary at the Paris sites if the prescribed geometric and optical properties were varied. Note that, in this section, we are only modifying properties within the WBGT calculation, so any changes to the distribution of radiation within the canyon will not impact the meteorological conditions. For a full comparison, we would repeat the 48-hour model run for each sensitivity test—however, this is impractical within the remit of this study, as hectometric simulations are so computationally expensive.

Modifying the building height influences the period of time that the globe is illuminated by the Sun (Figure 7): increasing building height results in shorter periods of illumination, while decreasing building height results in longer periods, with the greatest impacts at the narrower canyon sites. For flat-surface calculations, the globe is illuminated all day, with an enhancement of WBGT by up to 4 °C with respect to shaded conditions at the same time within a street canyon. Figure 7 also demonstrates the impact of radiation trapping within a canyon: in the narrower canyons (most notably at RDR and BSG while the globe is illuminated), WBGT is enhanced when canyon walls are included in the calculation. The difference between the flat-surface and full-height calculations at BSG in the middle of the day is about 0.5 °C. Both results highlight the importance of including the canyon geometry in urban heat stress calculations.

Modifying the optical properties (shortwave albedo and longwave emissivity) affects the amount of radiation incident on the globe and hence influences the magnitude of the WBGT. Figure 8 demonstrates the impact on WBGT of varying the wall and road albedo. We select representative high and low values of wall and road albedo based on a list of optical properties of different building materials in table C1 of Kotthaus *et al.* (2014). During periods of direct illumination, the range of representative wall albedos produces a 2 °C variation in WBGT, much greater than the influence of the road albedo range (much less than 1 °C). Two factors contribute to this: first, modifying wall albedo affects two out of the four facets rather than one; second, the range of plausible wall albedo values is greater. We also find a similar sensitivity of WBGT to wall albedo when the globe is shaded, implying that, while lighter walls may act to keep buildings cooler, they could lead to enhanced heat stress in the street during the daytime (echoing the result of Lee & Mayer, 2018).

At AMGI, PV, and QAF (figures not shown), the sensitivity of WBGT to wall albedo is much lower (less than

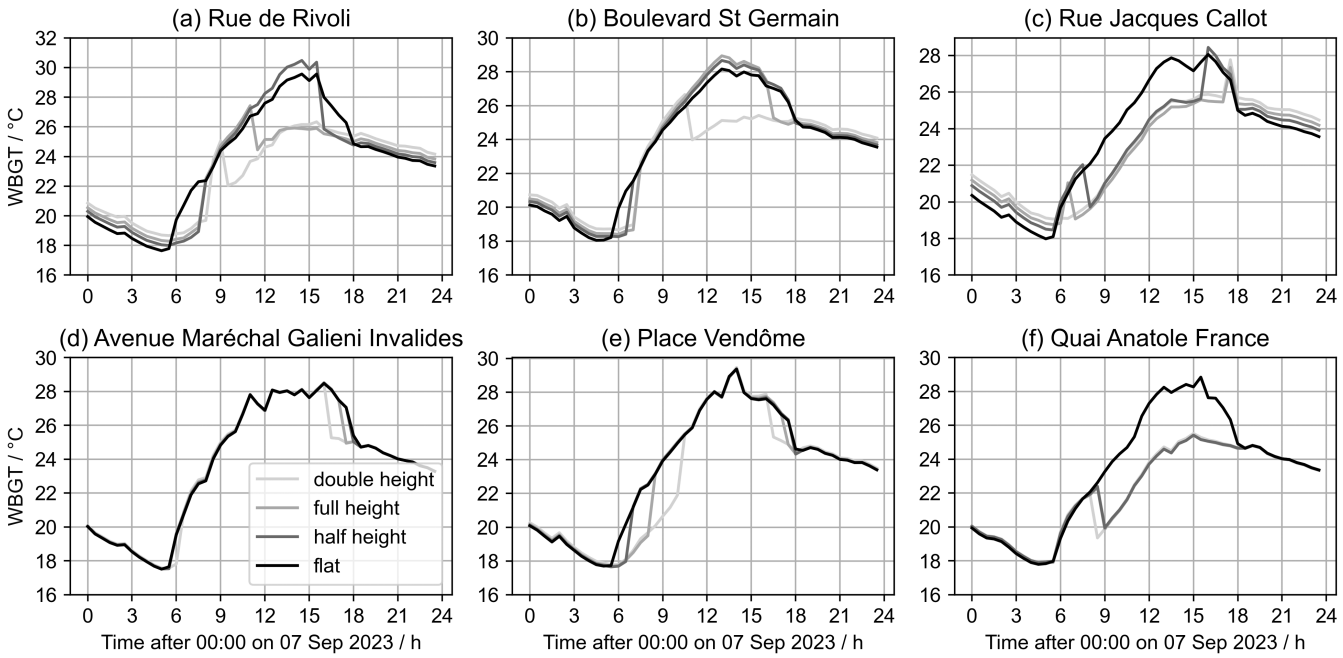

FIGURE 7 Time series of WBGT at the six sites, calculated using NWP model meteorology and fluxes and best estimates of canyon morphology, but with the canyon height modified at each site: either doubled, halved, or set to zero (creating a flat surface with no shading).

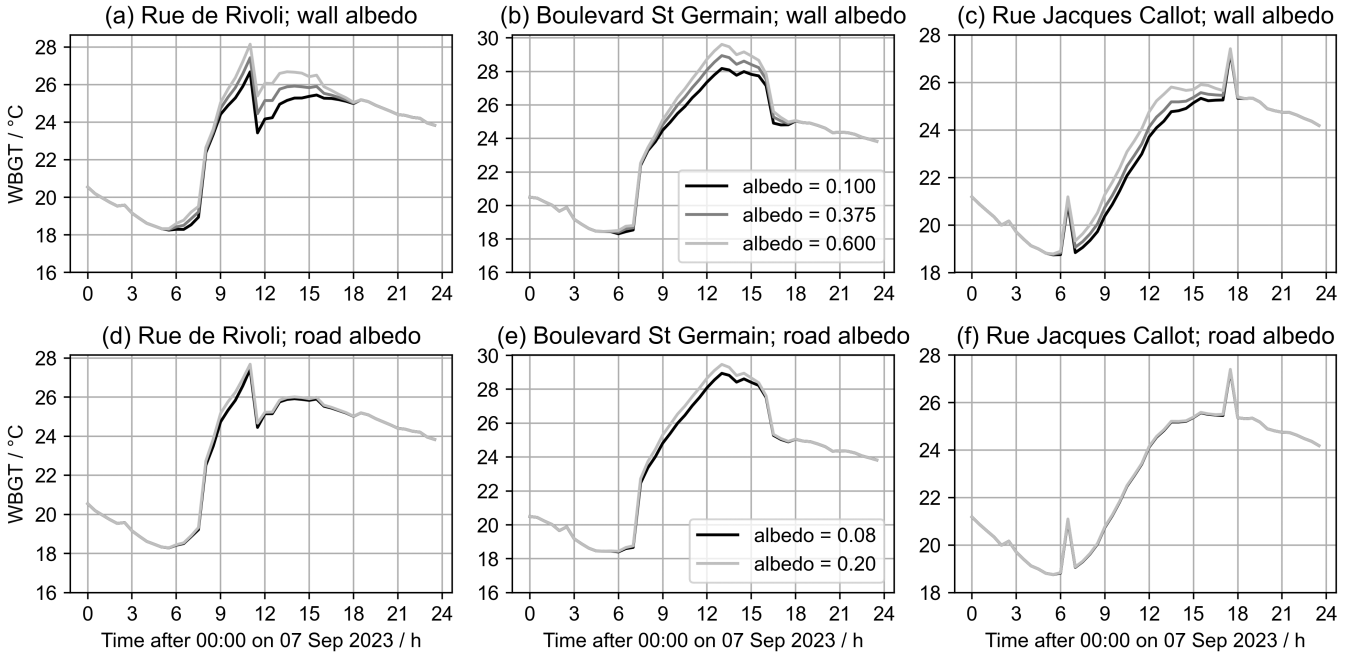

FIGURE 8 Time series of WBGT at three of the Paris sites, calculated using NWP model meteorology and fluxes and best estimates of canyon morphology, but with wall albedo (top row) and road albedo (bottom row) varied over a range of plausible wall and road building materials, based on data presented by Kotthaus *et al.* (2014).

0.1 °C across the range), with a slightly greater sensitivity to road albedo (up to 0.5 °C in the middle of the day). The impact on WBGT of modifying the wall and road emissivity (again based on high and low typical values as presented in Kotthaus *et al.*, 2014; figures not shown) is also small, with all impacts being less than 0.5 °C in magnitude at all sites.

Figure 9 demonstrates the sensitivity of the WBGT calculation at the RDR site to the main meteorological input variables. We present only results from RDR for this part of the analysis, as the model WBGT indicates both substantial sunny and shady periods during the day—sensitivities at other sites are similar. Raising or lowering the air temperature by 5 °C has a similar effect to doubling or halving the specific humidity, respectively, both producing a WBGT response in the range 3–5 °C at all times of day and night, with warmer and moister conditions leading to higher heat stress. Changes to the wind speed affect the black-globe temperature term, hence the greatest impacts are during sunny periods. Reducing the wind speed to $0.15\,\mathrm{m}\cdot\mathrm{s}^{-1}$ (the lowest wind speed for which the WBGT method applies) increases WBGT by about 2 °C during sunny periods; increasing it to $10\,\mathrm{m}\cdot\mathrm{s}^{-1}$ (a very windy day) reduces the WBGT by about 4 °C, enough to offset the impact of the direct illumination. WBGT is relatively insensitive to the surface temperature—a 5 °C variation results in a WBGT change of order 0.5 °C (an order of magnitude smaller than the effect of a similar change in air temperature).

The relative sensitivities of WBGT to the different meteorological quantities can largely be explained by the UCanWBGT equations. The stronger sensitivity to temperature and humidity reflects the higher weighting of WBGT to wet-bulb temperature, which is controlled by these quantities. In contrast, surface temperature influences WBGT via modifications to the longwave emission from the canyon walls and road, a small fraction of which is incident on the globe. The result is an enhancement of MRT and hence black-globe temperature, which has a lower weighting in the WBGT calculation.

Finally, Figure 10 shows the impact of limiting the number of shortwave and longwave reflections to two. In the case with the standard facet albedos (with a wall albedo of 0.375), the first reflection adds between 0.6 and 1.2 °C to the WBGT, while the contribution of the second reflection is about an order of magnitude smaller (0.1 °C). By analogy, we might expect the contribution from third-order reflections to add about 0.01 °C, which is a small change given the sensitivity of the WBGT calculation to the other properties presented in this section.

To challenge the limitation of two reflections, we repeat the sensitivity experiment with more reflective

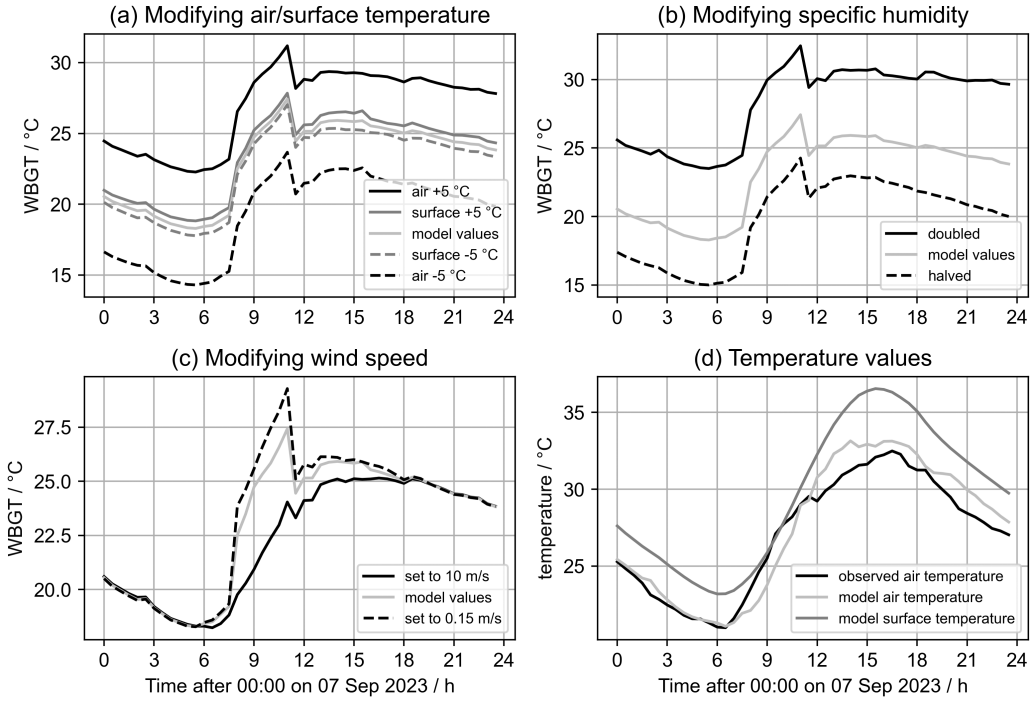

FIGURE 9 Time series of WBGT at Rue de Rivoli, showing sensitivity of the WBGT calculation to meteorological input fields: (a) air and surface temperature, (b) relative humidity, and (c) wind speed. See legends for the modifications applied to the field in each case. Panel (d) compares the observed air temperature with the model air and surface temperatures.

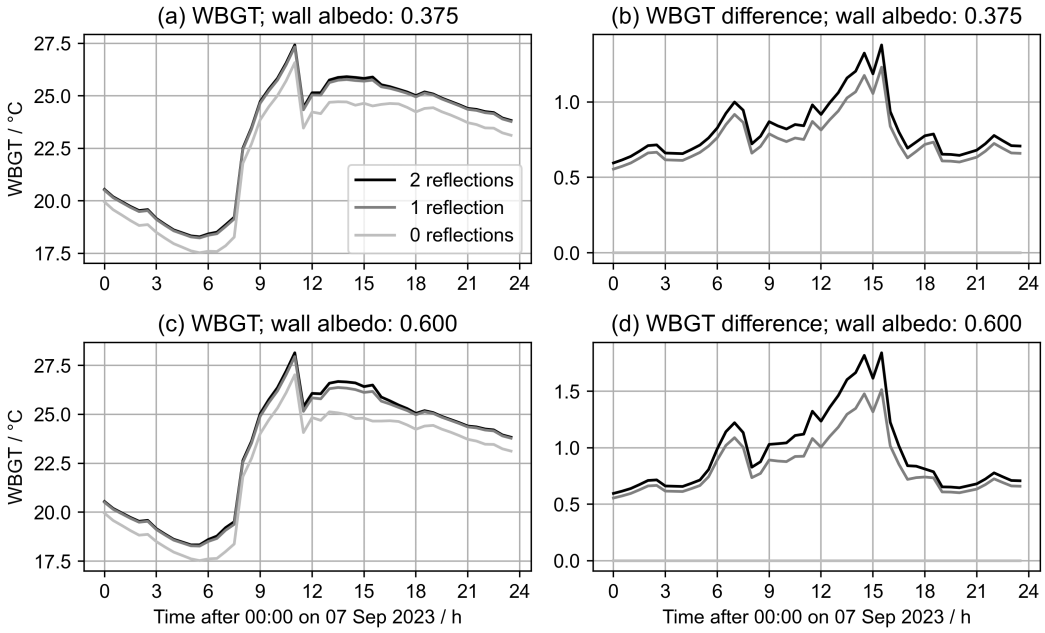

FIGURE 10 Time series of WBGT at Rue de Rivoli, showing the impact of modifying the number of reflections used in the calculation of MRT. Values of WBGT are shown in panels (a) and (c); differences from the zero-reflection case are shown in panels (b) and (d). Two choices of wall albedo are shown: 0.375 (top row) and 0.6 (bottom row).

walls, increasing their albedo to 0.6 (a reflective building material albedo according to Kotthaus *et al.*, 2014). With no shortwave influence overnight, the contributions remain the same. During the day, the first reflection adds about 1 °C to the WBGT, while the second adds 0.3 °C (about a third)—again, by analogy, we may expect a third reflection to add about 0.1 °C. This is still small compared with some of the sensitivities, although it may start to be problematic for surfaces that are more reflective than this.

4 | DEMONSTRATION: 2024 PARIS OLYMPIC MARATHON

In this section, we apply UCanWBGT to high-resolution model data to demonstrate how it could be used to provide safety advice to the organisers of sporting events. The marathon events at the Paris 2024 Olympic Games were scheduled for the final weekend, with three events held—the men's event on the morning of August 10 and the women's event on the morning of August 11 (both starting at 0800 local time; 0600 UTC), and the "*Marathon Pour Tous*" on the evening of August 10 (starting at 2100 local time; 1900 UTC). From the perspective of heat stress, the marathon event is the one that is most dependent on the weather, as the exertion of the runners is spread over a long period, as is the exposure to meteorological conditions.

4.1 | Marathon data

We ran another simulation using the Met Office Unified Model, this time starting at 1200 UTC on August 9, 2024 and running for 48 hours (allowing spin-up as before and spanning the whole of August 10, which featured two of the three marathon events). No other changes were made to the model configuration described in Section 3.2. In this section, we refer to August 10, 2024 as the "marathon day" and September 7, 2023 as the "heatwave day".

We present WBGT calculations in this section using both approaches highlighted in Section 2.8. First, we calculate WBGT along the marathon route. The route is provided as a series of longitude and latitude coordinates with varying spacing. From these coordinates, we split the route into "segments" that are 100 m long (to reflect the model grid length) and define the canyon orientation angle from the alignment of the route at the midpoint of each segment. We extract the meteorological fields, radiative fluxes, surface geometry, optical properties, and dominant surface type for each segment from the nearest grid point on the 100 m grid. For route segments classified as urban, we assume the runners to be running along the middle of the canyon (that is, $X = 0$ m and $Z = 1.5$ m) and calculate WBGT using a canyon morphology.

For most types of non-urban surface, we calculate WBGT using a flat-surface approach, although this is not appropriate for all surface types. Outside the city, most of the marathon route runs along roads through forests—runners are therefore, in essence, running through a "forest canyon" and certainly not across a flat surface. In the long term, we aim to develop a method to calculate MRT and hence WBGT under a forest canopy using a set of analytical equations of complexity comparable with UCanWBGT—however, that is beyond the scope of this study. We therefore take a simple approach and model forest segments as canyons using the same UCanWBGT formulation as for urban areas, but with the wall albedo and emissivity values set to those of trees. We set the canyon dimensions to be 15 m wide and 20 m deep, following typical dimensions of forest canyons along the roads of the marathon route based on analysis using Google Earth.

Second, we calculate a map of WBGT over the entire Paris domain using data from the high-resolution 100 m model. Meteorological fields, radiative fluxes, surface geometry, and optical properties are all taken from the model data. At each grid point, we assign the surface to be the dominant JULES surface type. As canyon orientation is not specified over the model domain, we perform a WBGT calculation averaging over three canyon orientation angles to represent random canyon alignment. For each orientation, we also calculate WBGT as an average over five globe positions distributed evenly across the width of the canyon. At forest grid points, we use the same approach but assuming randomly aligned forest roads of the same dimensions as above. At all other grid points, we calculate WBGT using a flat-surface approach.

Figure 11a shows a map of the dominant surface type across the Paris area with the marathon route indicated. For the analysis in this section, we subdivide the urban segments into "sparse urban" (any urban surface and a building height-to-width ratio of less than 0.75) and "dense urban" (as above, but with a height-to-width ratio of greater than or equal to 0.75). The threshold between dense and sparse urban is based on $H/W = 0.75$ being a common boundary between local climate zones (see table 3 of Stewart & Oke, 2012). From the perspective of UCanWBGT, there is no distinction in the WBGT calculation method across these two urban surface classes; the separation is only applied for analysis purposes. All other parts of the route are referred to in this section as "non-urban".

4.2 | Considerations around timing

Figure 11b shows the WBGT in the morning (at 0800 UTC). With the Sun low in the sky, the impact of shading from buildings is clear—in urban areas, the lowest WBGT values align with the dense urban areas towards the city centre, where street-level shading is greatest; higher WBGT values are in the suburbs, where the building aspect ratio is smaller. Outside the city, shading leads to lower WBGT in forest areas, while higher WBGT values are found in areas dominated by grassland. By 1200 UTC (near solar noon; Figure 11c) the Sun is higher, so the

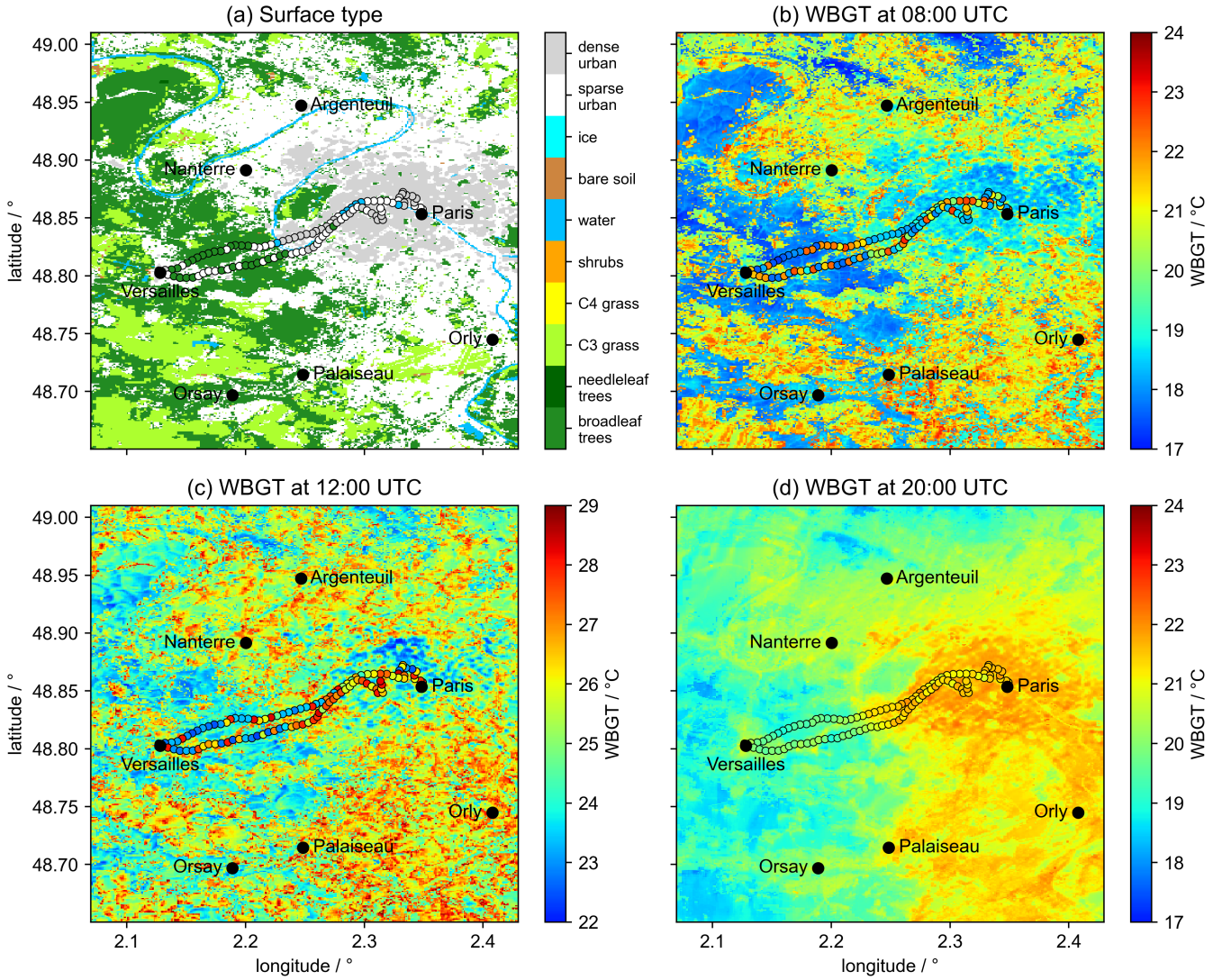

FIGURE 11 Maps of (a) dominant land-surface type for the Paris area, centred on the marathon route, and maps of WBGT derived from NWP model data from August 10, 2024 (b) in the morning (0800 UTC; 1000 local time), (c) near solar noon (1200 UTC; 1400 local time), and (d) in the evening after sunset (2000 UTC; 22:00 local time). Calculated values along the marathon route are indicated on all subplots (circles). Selected place names have been added for context. [Colour figure can be viewed at wileyonlinelibrary.com]

degree of shading is much reduced—WBGT values are generally high across the whole domain, with shading only evident to any great extent where the deepest canyons exist (in the centre of the city and in the forests). At night (2000 UTC; Figure 11d), temperature differences between the urban and non-urban areas lead to an urban heat island in WBGT, with urban areas of order 2 °C higher than the surrounding countryside.

Figure 12a shows the diurnal evolution of WBGT as a histogram along the route. Values start at a minimum value at sunrise (around 16 °C), rising through the morning as the Sun illuminates more of the surface. Maximum WBGT is reached in the early afternoon—a wider range of WBGT values (from about 23–29 °C) associated with different degrees of heating of the various surface types. Throughout much of the day, the histogram has two branches—a warmer branch containing illuminated surfaces (centred on 23 °C at 0900 UTC) and a cooler branch containing shaded surfaces (centred on 20 °C at 0900 UTC).

The levels of WBGT risk to distance runners according to Armstrong *et al.* (1996) are included in Figure 12. For the purpose of this demonstration, let us assume we are providing organisers of the event with heat stress forecasts and the aim is to avoid exposing the runners to conditions with a WBGT of greater than 23 °C (high risk or above). Between 0800 and 1900 UTC, parts of the route experience WBGT values above this threshold, so the recommendation would be that the marathon events should not be in progress during this period.

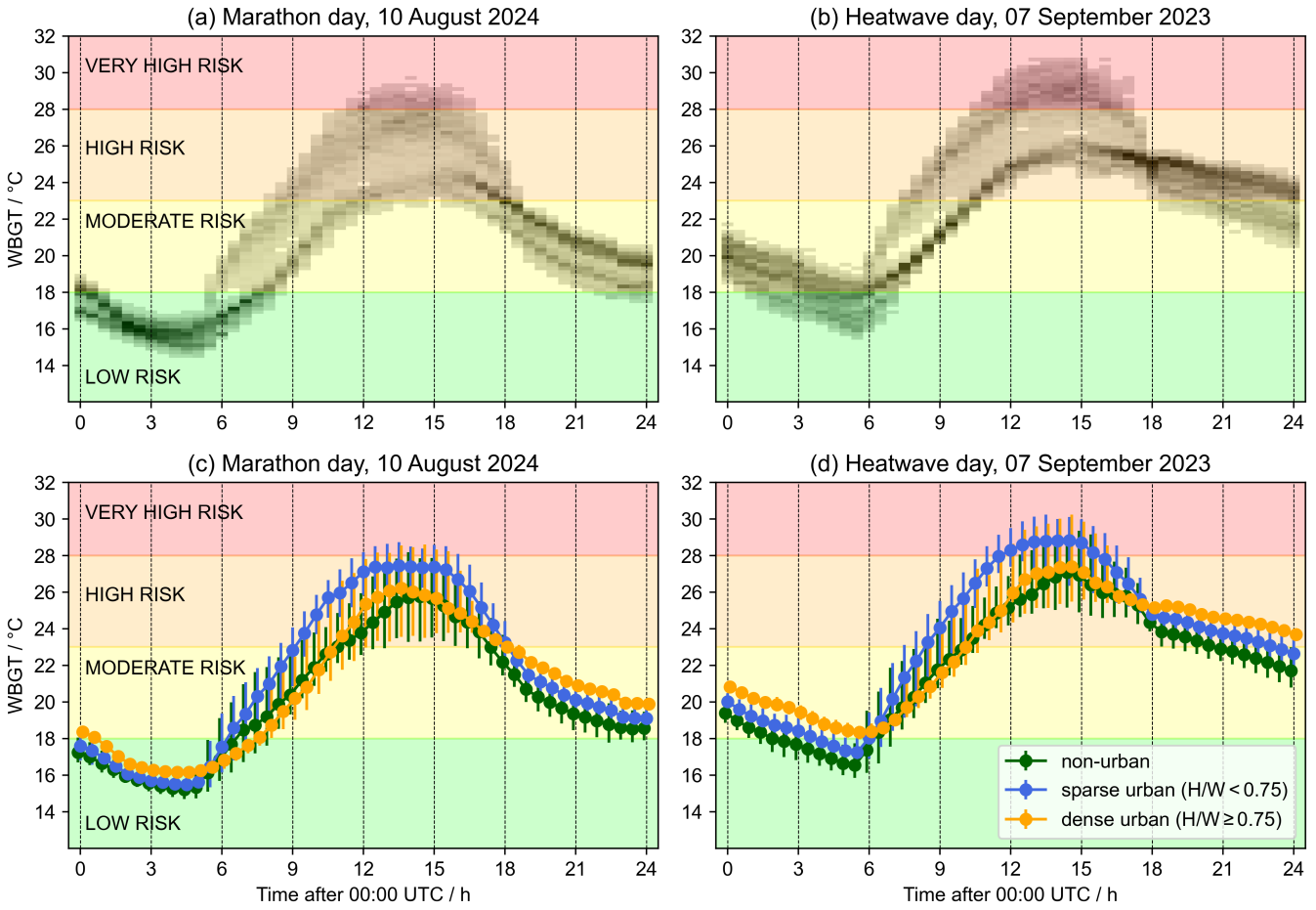

FIGURE 12 Distributions of WBGT along the route over the course of (a, c) the marathon day, August 10, 2024 and (b, d) the heatwave day, September 7, 2023. The grey shading in panels (a) and (b) shows histograms of WBGT along the route at each 30-minute interval. Lines in panels (c) and (d) indicate the mean WBGT along the route for three surface categories—dense urban, sparse urban, and non-urban (all other surfaces); bars indicate the 10th and 90th percentiles of WBGT across that surface type. Bars are slightly offset horizontally for clarity. Background shading on all panels indicates the WBGT risk thresholds set by the American College of Sports Medicine (Armstrong *et al.*, 1996). [Colour figure can be viewed at wileyonlinelibrary.com]

Figure 13a shows the distribution of WBGT throughout the day as a function of distance along the route, coloured by the WBGT risk ranges as in Figure 12. The lines indicate the paths runners would take across the plot for different marathon times. Along much of the route, high-risk conditions set in at about 1000 UTC. Hence, a 0600 UTC start (when the marathon really started) gives the runners four hours to complete the course without a great deal of exposure to high-risk WBGT values (note that, in the elite event, most runners took between two and three hours to complete the course). Similarly, for the evening event, the high-risk conditions have generally subsided over the whole route at about 1800 UTC, hence a start time of 1900 UTC avoids any instances of high risk and the risk levels fall further into the night.

For context, Figures 12b and 13b show the levels of WBGT risk runners would be exposed to if the same Olympic events had been held on the heatwave day (September 7, 2023). Overall, this was a hotter day than the actual marathon day, with maximum WBGT values about 2 °C higher. In this example, the high-risk conditions start about an hour earlier (around 0900 UTC), so a 0600 UTC start may have exposed runners to high risk towards the end of the course, implying the need for an earlier start. In the evening, high-risk conditions near the start and end of the route persist until midnight, suggesting that, had the *Marathon Pour Tous* been held on the heatwave day, it would not have been safe to start until the early hours of the following morning.

4.3 | Considerations around the route

Lines in Figure 12c,d indicate the mean WBGT throughout the day across each of three classes of surface type: dense urban and sparse urban (see Section 4.1 for definitions),

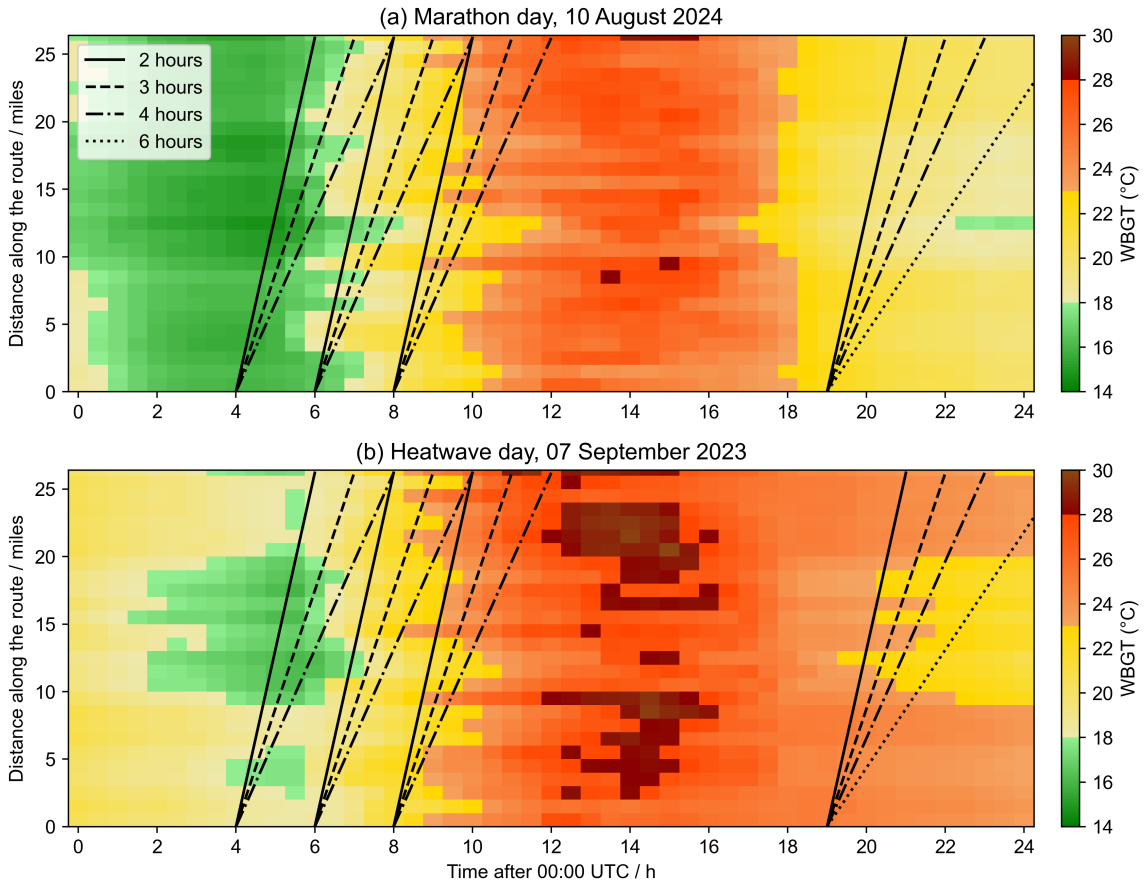

FIGURE 13 WBGT along the route during the day. Estimates of WBGT have been averaged into mile-long sections and plotted for each half hour of the day. The colour bar is stepped to indicate the WBGT thresholds as presented in Figure 12. Lines across the chart indicate the trajectory across the graph that would be taken by a runner completing the marathon over different race times, assuming running at a constant speed (see legend). [Colour figure can be viewed at wileyonlinelibrary.com]

and non-urban (any other surface type—mostly forests). During the morning, the WBGT over sparse urban parts of the course rises more rapidly, as the surfaces are less shaded, while the WBGT rise in dense urban and forest areas is less rapid. Through the middle of the day, as the urban canyons heat up, more radiation is emitted into the canyons and the sparse urban areas continue to experience a higher WBGT than non-urban areas. Dense urban areas retain lower WBGT, as shading is still a dominant factor. Urban heat storage continues into the evening and night, with the urban heat island seen in Figure 11d clearly visible in the route data, with dense urban areas retaining the highest WBGT values overnight and non-urban areas having lower values.

For a daytime event, segments of the route through dense urban and forest areas provide the most shading and lower WBGT values overall. Across both case-study days, the mean WBGT across these parts of the route is up to 3 °C lower than the mean values in sparse urban or non-urban parts, with the greatest differences in the morning and afternoon, when the Sun is lower and more likely to be behind buildings or trees. For a nighttime event, however, the dense urban parts of the route have a WBGT 2–3 °C higher than non-urban parts, with greater differences on the heatwave day, when the daytime temperatures were higher.

The advice for race organisers would therefore be to suggest that, if the event is being run at a time of year when heatwave conditions may occur, maximising the fraction of race distance in dense urban and forest areas would increase the viability of a daytime event being safe to run and allow for later start times. Based on the timings from the case studies presented here, the 23 °C threshold is passed about two hours later in these areas than elsewhere. An extra safety consideration would be to ensure a larger fraction of the end of the route was in dense urban areas for a morning marathon, to provide relief from direct illumination when heat stress is higher. Conversely, for a nighttime event, maximising course distance outside urban areas would reduce heat stress on the runners. In the heatwave case study, a route that is mostly non-urban would be safe to run over three hours earlier than a route that was mostly in dense urban areas.

5 | DISCUSSIONS

UCanWBGT is a computationally efficient method to calculate WBGT in urban areas using standard NWP model fields. It represents the urban area as infinitely long street canyons and accounts for the transfer of radiation between canyon facets, allowing calculation of WBGT for a black globe located anywhere in the canyon. We have designed the method to be versatile and it can be used to calculate WBGT at specific locations where the canyon geometry and optical properties are known, or over whole NWP model domains where either properties are prescribed from model input data or, in the case of canyon alignment, an average must be taken over values. The canyon morphology allows UCanWBGT to capture the shading of direct shortwave radiation during the day and enhanced longwave warming during the night, both of which would not be represented using a flat plane approximation such as that of Di Napoli *et al.* (2020). Figure 14 demonstrates the impact of including canyon walls in the WBGT calculation over Paris: daytime shading reduces WBGT by up to 4.5 °C, while nighttime warming enhances it by up to 1.5 °C, with the greatest impact in urban and forested areas.

In comparisons with WBGT estimates from black-globe measurements at street level in Paris, we demonstrated that UCanWBGT can produce high-quality representations of WBGT in street canyons when using NWP model output. In the heatwave case study (September 7, 2023), UCanWBGT reproduced daily trends in observed WBGT and, despite some errors associated with real-world canyon morphology not matching that of an idealised canyon, it captured the steps in WBGT associated with the transition between the black globe being illuminated by the Sun and shaded from it. Much of the difference between model and observations was associated with forecast errors in the model meteorological fields.

To provide robust, reliable forecasts of heat stress using UCanWBGT, there are two main considerations. First, the urban surface data must be suitably representative of the area: inaccurate geometry can lead to errors in the duration of illumination to direct sunlight, which is a dominant factor in determining the WBGT; poor choices of albedo or emissivity can bias the WBGT high or low. When running UCanWBGT over a large area, there is therefore a need for the best land-surface dataset available, with a realistic representation of urban surface heterogeneity, such as WorldCover. Ongoing development of high-resolution land-surface datasets will be beneficial to models such as UCanWBGT.

Meteorological data must also be selected carefully to provide realistic WBGT forecasts. We showed in Section 3 that forecast errors were a contributing factor to the differences between model and observed WBGT, and demonstrated the sensitivity of WBGT estimates to the driving meteorological fields. We must ensure that the meteorological fields extracted from the NWP model are representative of those fields within the canyons. In this study, we have defined the 1.5 m temperature, humidity, and wind speed to be representative of values at street level. Figure 5 shows that these properties reflect the observed conditions well, although they are calculated from surface values using Monin–Obukhov theory, which does not apply within the canyons. Care is also needed with the

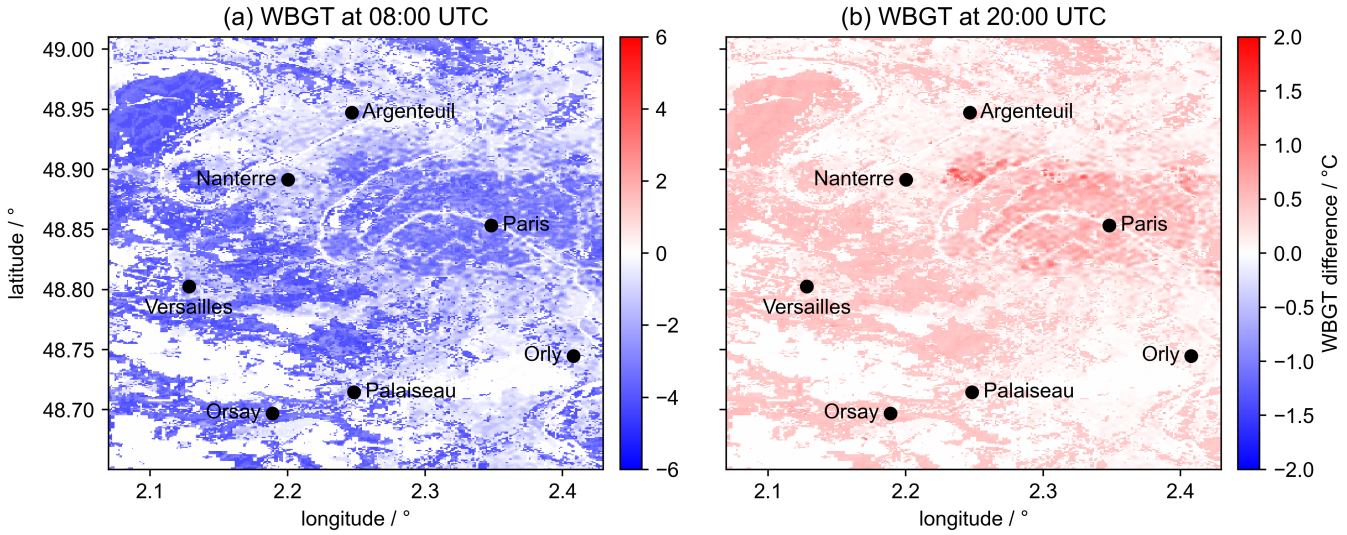

FIGURE 14 Maps of the difference in WBGT over the Paris area when calculated with a flat-surface geometry and with a full canyon geometry for the marathon day (August 10, 2024) at (a) 0800 UTC and (b) 2000 UTC. WBGT values are calculated from NWP model data with UCanWBGT, following the same approach as used for Figure 11. [Colour figure can be viewed at wileyonlinelibrary.com]

surface temperature term, as this can be defined in many ways—in our study, we used the surface temperature from the urban canyon tile, as this was available in our model data, although, if only a grid-box mean surface temperature is provided, some degree of urban surface temperature proxy may be needed. If surface temperature is unavailable, a simple approach is to use air temperature in its place. The two are not the same—see Figure 9d for a comparison at Rue de Rivoli on the heatwave day—but we show in the same figure that a surface temperature error of that magnitude would impact WBGT estimates by less than 0.5 °C.

Our approach has been dedicated to improving WBGT estimates in urban areas, and this study has evaluated its performance in urban areas. We recognise that there are many potential future developments for UCanWBGT to further enhance its use that are beyond the scope of this study. To capture the effects of shading in the forested parts of the marathon route, we introduced a simple forest canopy model based on the urban canyon. A more sophisticated model could be developed, whereby the leaves apply a shading effect dependent on leaf-area index, with radiative interactions between the ground and the canopy accounted for. Using the same viewing fraction arguments, a set of analytical equations could easily be generated. A similar approach could be taken in urban areas to account for trees in streets—care would be needed to ensure that the representation approach remains mathematically simple, but this could be used to investigate the effect of urban trees on heat stress.

We also demonstrated UCanWBGT in action by indicating how forecasts of WBGT could be used to inform event organisers about the safety and routing of long-distance running events. It should be borne in mind that the demonstration only considers a single event and two case-study days. A more detailed and informative approach to event planning could be to calculate WBGT over the route for a range of days based on the climatology of the area at the time of the event (for example, the same month) and build up more detailed statistics. In the days building up to the event, providing forecasts further in advance could give organisers an indication of whether the start time needs to be modified. Further applications of UCanWBGT could be explored, including other types of sporting event, impacts on manual workers, or urban design, such as designing cool outdoor spaces.

6 | SUMMARY AND CONCLUSIONS

In this study, we presented a model, "UCanWBGT", that determines heat stress in an urban environment. It is designed to be computationally efficient, using analytical equations to calculate the radiative transfer within an infinitely long street canyon with up to two reflections between facets permitted. Heat stress is then calculated in the form of wet-bulb globe temperature (WBGT) using a standard set of empirical equations. The approach uses a standard set of meteorological fields that would typically be output from weather or climate models. The properties of the urban surface (geometry and optical properties) may be either prescribed if known, allowing WBGT calculations at specific locations, or extracted from model input fields, permitting calculations over wide areas. Its design and versatility allow it to be suitable for use within both numerical weather prediction (NWP) and climate model simulations.

For validation, we used UCanWBGT to determine estimates of WBGT from output data from a high-resolution NWP simulation over the Paris area. We compared these estimates with WBGT values calculated from observations made using black-globe thermometers situated within street canyons in Paris as part of the PANAME project on a sunny heatwave day (September 7, 2023). We found that UCanWBGT captures daily variations and trends in WBGT well and can represent the difference when the globe is illuminated by the Sun or shaded by buildings. Deviations between observations and model WBGT were associated with forecast errors in meteorological fields (in particular, temperature and humidity) and features of the real-world locations in Paris differing from the idealised canyon morphology.

We showed the sensitivity of the model to both geometric and optical properties. Modifying the canyon geometry (building height) affects the timing of sunny and shady periods; modifying the optical properties (wall and road albedo and emissivity) affects the total radiation incident on the globe. We also demonstrated the sensitivity of WBGT estimates to the meteorological fields, suggesting that model errors could impact the WBGT predictions, especially temperature and humidity, as the wet-bulb temperature term has a higher weighting in the WBGT equation. We also demonstrated that our choice to limit the number of diffuse reflections to two has a small impact on WBGT estimates over a wall albedo range spanning typical building materials.

We concluded by demonstrating how WBGT estimates from UCanWBGT could be used to provide safety information to organisers of sporting events. Using a high-resolution NWP simulation of August 10, 2024 (a day featuring two of the three marathon events at the 2024 Paris Olympics), we calculated WBGT both over the general Paris area and specifically along the marathon route and drafted a set of hypothetical recommendations for the organisers about the timing and routing of an event

that would minimise heat stress impacts on the athletes. By comparing WBGT with published safety thresholds, we proposed time limits by which a morning event (the men's marathon) should be completed, and after which an overnight event (the *Marathon Pour Tous*) could safely start. We also partitioned the route based on the surface type and showed that, for a daytime event, lower heat stress is experienced in city centres (dense urban areas) and forest roads, while for a nighttime event countryside (non-urban) areas are favourable to reduce heat stress.

The crucial contribution of UCanWBGT in comparison with the flat-plane method of Di Napoli *et al.* (2020) is the impact of including the canyon morphology in the radiative transfer calculations. During the day, shading of shortwave direct radiation within the canyon reduces WBGT by up to 4.5 °C; at night, longwave emissions from the canyon walls enhance WBGT by up to 1.5 °C. In the case of the marathon, excluding these effects would impact the message about the safe timings of the event heavily. It is clear (as Di Napoli *et al.*, 2020., recognise) that a flat-surface approximation is not suited to an urban area and UCanWBGT provides a simple, computationally efficient solution.

ACKNOWLEDGEMENTS

We thank Huw Lewis, Belinda Roux, Cassandra Rogers, and two anonymous reviewers for comments and feedback on our article. We also thank Aude Lemonsu and Guillaume Dumas for contributions to arranging and providing the PANAME data used in this study. The contributions of J. Shonk to this work were funded by the Met Office Weather and Climate Science for Service Partnership (WCSSP) India project, which is supported by the UK Department for Science, Innovation and Technology (DSIT). L. Blunn was funded by the Met Office AI4 Climate project, which is also supported by DSIT. This work contributed to and benefitted from the Paris 2024 Olympics Research Demonstration Project, coordinated by Météo-France and endorsed by the World Meteorological Organization. Base maps in Figure 4 © OpenStreetMap; see https://www.openstreetmap.org/copyright/.

CONFLICT OF INTEREST STATEMENT

The authors declare no conflict of interest.

DATA AVAILABILITY STATEMENT

The UCanWBGT computer code is available in a Github repository, along with the relevant data fields used to recreate the figures in this study: https://github.com/MetOffice/UCanWBGT.

ORCID

Jonathan K. P. Shonk https://orcid.org/0000-0003-0479-7590
Lewis P. Blunn https://orcid.org/0000-0002-3207-5002
Vinod Kumar https://orcid.org/0000-0002-7395-4548
Jean Wurtz https://orcid.org/0000-0002-8195-3537

REFERENCES

Aadhar, S. & Mishra, V. (2023) The 2022 mega heatwave in South Asia in the observed and projected future climate. *Environmental Research Letters*, 18, 104,011.

Armstrong, L.E., Epstein, Y., Greenleaf, J.E., Haymes, E.M., Hubbard, R.W., Roberts, W.O. et al. (1996) American College of Sports Medicine position stand: heat and cold illnesses during distance running. *Medicine and Science in Sports and Exercise*, 28(12), 1–10.

Best, M.J., Pryor, M., Clark, D.B., Rooney, G.G., Essery, R.L.H., Ménard, C.B. et al. (2011) The Joint UK Land Environment Simulator (JULES), model description - Part 1: energy and water fluxes. *Geoscientific Model Development*, 4, 677–699.

Błazejczyk, K., Epstein, Y., Jendritzky, G., Staiger, H. & Tinz, B. (2012) Comparison of UTCI to selected thermal indices. *International Journal of Biometeorology*, 56, 515–532.

Bocher, E., Petit, G., Bernard, J. & Palominos, S. (2018) A geoprocessing framework to compute urban indicators: the MApUCE tools chain. *Urban Climate*, 24, 153–174.

Bontemps, S., Defourny, P., Radoux, J., Van Bogaert, E., Lamarche, C., Achard, F. et al. (2013) Consistent global land cover maps for climate modelling communities: current achievements of the ESA's land cover CCI. In: *Proceedings of the ESA Living Planet Symposium*, Vol. 13. Edinburgh, UK: European Space Agency, pp. 9–13.

Bruse, M. (1999) *Entwicklung des prognostischen numerischen Modells ENVI-met zur Simulation der Wind-, Temperatur- und Feuchteverteilung in städtischen Strukturen*. PhD thesis, Ruhr-Universität Bochum.

Bush, M., Flack, D.L.A., Lewis, H.W., Bohnenstengel, S.I., Short, C.J., Franklin, C. et al. (2025) The third Met Office Unified Model–JULES Regional Atmosphere and Land configuration, RAL3. *Geoscientific Model Development Discussions*, 18, 3819–3855.

Buzan, J.R., Oleson, K. & Huber, M. (2015) Implementation and comparison of a suite of heat stress metrics within the Community Land Model version 4.5. *Geoscientific Model Development*, 8, 151–170.

Campbell, S., Remenyi, T.A., White, C.J. & Johnston, F.H. (2018) Heatwave and health impact research: a global review. *Health and Place*, 53, 210–218.

Clark, D.B., Mercado, L.M., Sitch, S., Jones, C.D., Gedney, N., Best, M.J. et al. (2011) The Joint UK Land Environment Simulator (JULES), model description - Part 2: carbon fluxes and vegetation dynamics. *Geoscientific Model Development*, 4, 701–722.

De Lieto Vollaro, R., Vallati, A. & Botillo, S. (2013) Differents [sic] methods to estimate the mean radiant temperature in an urban canyon. *Advanced Materials Research*, 650, 647–651.

Di Napoli, C., Hogan, R.J. & Pappenberger, F. (2020) Mean radiant temperature from global-scale numerical weather

prediction models. *International Journal of Biometeorology*, 64, 1233–1245.

Fanger, P.O. (1972) *Thermal comfort: analysis and application in environmental engineering*. New York: McGraw Hill.

Fiala, D., Havenith, G., Bröde, P., Kampmann, B. & Jendritzky, G. (2012) UTCI-Fiala multi-node model of human heat transfer and temperature regulation. *International Journal of Biometeorology*, 56, 429–441.

Fiala, D., Psikuta, A., Jendritzky, G., Paulke, S., Nelson, D., van Marken Lichtenbelt, W. et al. (2010) Physiological modelling for technical, clinical and research applications. *Frontiers in Bioscience*, S2, 939–968.

Fischereit, J. (2021) The simple urban radiation model for estimating mean radiant temperature in idealised street canyons. *Urban Climate*, 35(100694), 100694.

García-Herrera, R., Díaz, J., Trigo, R.M., Luterbacher, J. & Fischer, E.M. (2010) A review of the European summer heat wave of 2003. *Critical Reviews in Environmental Science and Technology*, 40, 267–306.

Harman, I.N., Best, M.J. & Belcher, S.E. (2004) Radiative exchange in an urban street canyon. *Boundary-Layer Meteorology*, 110, 301–316.

Horton, R.M., Mankin, J.S., Lesk, C., Coffel, E. & Raymond, C. (2016) A review of recent advances in research on extreme heat events. *Current Climate Change Reports*, 2, 242–259.

IPCC. (2023) *Climate change 2023: synthesis report. Contribution of working groups I, II and III to the sixth assessment report of the intergovernmental panel on climate change*. Geneva, Switzerland: IPCC. Available from: https://doi.org/10.59327/IPCC/AR6-9789291691647

ISO 7243. (1989) Hot environments - estimation of the heat stress on working man, based on the WBGT index (Wet-Bulb Globe Temperature).

ISO 7726. (1998) Ergonomics of the thermal environment – instruments for measuring physical quantities.

Jendritzky, G. & Nübler, W. (1981) A model analysing the urban thermal environment in physiologically significant terms. *Archives for Meteorology, Geophysics and Bioclimatology*, 29, 313–326.

Johnson, G.T., Oke, T.R., Lyons, T.J., Steyn, D.G., Watson, I.D. & Voogt, J.A. (1991) Simulation of surface urban heat islands under ideal conditions at night. Part 1: theory and tests against field data. *Boundary-Layer Meteorology*, 56, 275–294.

Kántor, N. & Unger, J. (2011) The most problematic variable in the course of human biometeorological comfort assessment - the mean radiant temperature. *Open Geosciences*, 3, 90–100.

Kotthaus, S., Smith, T.E.L., Wooster, M.J. & Grimmond, C.S.B. (2014) Derivation of an urban materials spectral library through emittance and reflectance spectroscopy. *ISPRS Journal of Photogrammetry and Remote Sensing*, 94, 194–212.

Krayenhoff, E.S., Christen, A., Martilli, A. & Oke, T.R. (2014) A multi-layer radiation model for urban neighbourhoods with trees. *Boundary-Layer Meteorology*, 151, 139–178.

Krüger, E.L., Minella, F.O. & Matzarakis, A. (2014) Comparison of different methods of estimating the mean radiant temperature in outdoor thermal comfort studies. *International Journal of Biometeorology*, 58, 1727–1737.

Kusaka, H., Kondo, H., Kikegawa, Y. & Kimura, F. (2001) A simple single-layer urban canopy model for atmospheric models: comparison with multi-layer and slab models. *Boundary-Layer Meteorology*, 101, 329–358.

Lee, H. & Mayer, H. (2018) Thermal comfort of pedestrians in an urban street canyon is affected by increasing albedo of building walls. *International Journal of Biometeorology*, 62, 1199–1209.

Lemonsu, A., Barrau, S., Capo, J., Céspedes, J., Dahech, S., de Munck, C. et al. (2025) PANAME-Urban campaign: investigating multi-scale surface–atmosphere interactions and thermal contrasts in the Paris region (France). *Bulletin of the American Meteorological Society*.

Leroyer, S., Bélair, S., Spacek, L. & Gultepe, I. (2018) Modelling of radiation-based thermal stress indicators for urban numerical weather prediction. *Urban Climate*, 25, 64–81.

Lindberg, F., Holmer, B. & Thorsson, S. (2008) SOLWEIG 1.0 – modelling spatial variations of 3D radiant fluxes and mean radiant temperature in complex urban settings. *Urban Climate*, 25, 64–81.

Lipson, M.J., Grimmond, S., Best, M., Abramowitz, G., Coutts, A., Tapper, N. et al. (2024) Evaluation of 30 urban land surface models in the Urban-PLUMBER project: phase 1 results. *Quarterly Journal of the Royal Meteorological Society*, 150, 126–129.

Masson, V. (2000) A physically based scheme for the urban energy budget in atmospheric models. *Boundary-Layer Meteorology*, 94, 357–397.

Matzarakis, A., Rutz, F. & Mayer, H. (2010) Modelling radiation fluxes in simple and complex environments: basics of the RayMan model. *International Journal of Biometeorology*, 54, 131–139.

Meehl, G.A. & Tebaldi, C. (2004) More intense, more frequent, and longer lasting heat waves in the 21st century. *Science*, 305, 994–997.

Oleson, K.W., Bonan, G.B., Feddema, J., Vertenstein, M. & Grimmond, C.S.B. (2008) An urban parameterization for a global climate model. Part I: formulation and evaluation for two cities. *Journal of Applied Meteorology and Climatology*, 47, 1038–1060.

Park, C.Y., Lee, D.K., Krayenhoff, E.S., Heo, H.K., Ahn, S., Asawa, T. et al. (2018) A multilayer mean radiant temperature model for pedestrians in a street canyon with trees. *Building and Environment*, 141, 298–309.

Parsons, K. (2006) Heat stress standard ISO 7243 and its global application. *Industrial Health*, 44, 368–379.

Parsons, K. (2013) Occupational health impacts of climate change: current and future ISO standards for the assessment of heat stress. *Industrial Health*, 51, 86–100.

Porson, A., Clark, P.A., Harman, I., Best, M. & Belcher, S. (2010) Implementation of a new urban energy budget scheme in the MetUM. Part I: description and idealized simulations. *Quarterly Journal of the Royal Meteorological Society*, 136, 1514–1529.

Shaposhnikov, D., Revich, B., Bellander, T., Bedada, G.B., Bottai, M., Kharkova, T. et al. (2014) Mortality related to air pollution with the Moscow heat wave and wildfire of 2010. *Epidemiology*, 25, 359–364.

Sparrow, E.M. & Cess, R.D. (1978) *Radiation heat transfer*. California, US: Wadsworth Publishing Company.

Stewart, I.D. & Oke, T.R. (2012) Local climate zones for urban temperature studies. *Bulletin of the American Meteorological Society*, 9, 1879–1900.

Thorsson, S., Lindberg, F., Eliasson, I. & Holmer, B. (2007) Different methods for estimating the mean radiant temperature in an outdoor urban setting. *International Journal of Climatology*, 27, 1983–1993.

Wang, Z.H., Bou-Zeid, E. & Smith, J.A. (2013) A coupled energy transport and hydrological model for urban canopies evaluated using a wireless sensor network. *Quarterly Journal of the Meteorological Society*, 139(1), 1643–1657.

Warren, R.A. (2025) A consistent treatment of mixed-phase saturation for atmospheric thermodynamics. *Quarterly Journal of the Royal Meteorological Society*, 151, E4866.

Yaglou, C.P. & Minard, D. (1957) Control of heat casualties at military training centres. *American Medical Association Archives of Industrial Health*, 16, 302–316.

Zanaga, D., Van De Kerchove, R., De Keersmaecker, W., Souverijns, N., Brockmann, C., Quast, R. et al. (2021) ESA WorldCover 10 m 2020 v100.

How to cite this article: Shonk, J.K.P., Blunn, L.P., Kumar, V., Wurtz, J. & Masson, V. (2026) UCanWBGT: urban street canyon heat stress calculation for weather and climate models. *Quarterly Journal of the Royal Meteorological Society*, e70082. Available from: https://doi.org/10.1002/qj.70082